

IMMUNOLOGY

Redirecting raltitrexed from cancer cell thymidylate synthase to *Mycobacterium tuberculosis* phosphopantetheinyl transferase

Amrita Singh^{1†}, Samantha Ottavi^{2†}, Inna Krieger³, Kyle Planck⁴, Andrew Perkowski², Takushi Kaneko⁵, Andrew M. Davis⁶, Christine Suh¹, David Zhang¹, Laurent Goullieux⁷, Alexander Alex^{8,9}, Christine Roubert⁷, Mark Gardner⁸, Marian Preston⁶, Dave M. Smith⁶, Yan Ling¹, Julia Roberts¹, Bastien Cautain⁷, Anna Upton⁷, Christopher B. Cooper⁵, Natalya Serbina⁵, Zaid Tanvir⁵, John Mosior³, Ouathék Ouerfelli¹⁰, Guangli Yang¹⁰, Ben S. Gold¹, Kyu Y. Rhee⁴, James C. Sacchettini³, Nader Fotouhi^{5*}, Jeffrey Aubé^{2*}, Carl Nathan^{1*}

Copyright © 2024 The Authors, some rights reserved; exclusive licensee American Association for the Advancement of Science. No claim to original U.S. Government Works. Distributed under a Creative Commons Attribution NonCommercial License 4.0 (CC BY-NC).

There is a compelling need to find drugs active against *Mycobacterium tuberculosis* (*Mtb*). 4'-Phosphopantetheinyl transferase (PptT) is an essential enzyme in *Mtb* that has attracted interest as a potential drug target. We optimized a PptT assay, used it to screen 422,740 compounds, and identified raltitrexed, an antineoplastic antimetabolite, as the most potent PptT inhibitor yet reported. While trying unsuccessfully to improve raltitrexed's ability to kill *Mtb* and remove its ability to kill human cells, we learned three lessons that may help others developing antibiotics. First, binding of raltitrexed substantially changed the configuration of the PptT active site, complicating molecular modeling of analogs based on the unliganded crystal structure or the structure of cocrystals with inhibitors of another class. Second, minor changes in the raltitrexed molecule changed its target in *Mtb* from PptT to dihydrofolate reductase (DHFR). Third, the structure-activity relationship for over 800 raltitrexed analogs only became interpretable when we quantified and characterized the compounds' intrabacterial accumulation and transformation.

INTRODUCTION

The use of antibiotics in medical practice is becoming increasingly ineffective, a crisis often termed “antimicrobial resistance” (AMR) for one of its contributing factors (1–3). Accordingly, a growing number of academic laboratories, with the support of grants from national governments and charitable foundations, are engaging in early-stage antibiotic discovery, often in partnership with pharmaceutical companies (4, 5). These efforts are undertaken despite the grim estimate of Payne and colleagues (6) that the success rate in the pharmaceutical industry in recent decades has averaged 0.17% for passing through each successive stage of drug development from a high-throughput screening (HTS) campaign to the clinical launch of a new antibacterial agent. There are few reports of specific failures in these endeavors, reflecting the tendency of the scientific literature to report only what can be presented as a success. Yet, failures hold lessons that might increase the efficiency, if not the success, of other anti-infective discovery campaigns. Given the gravity of the crisis in AMR, such lessons should be shared.

The work reported here builds on the discovery of drug-like amidinouras that kill *Mycobacterium tuberculosis* (*Mtb*), the world's leading cause of death from infection before COVID-19, by inhibiting the essential enzyme PptT (7). PptT is essential for survival of *Mtb* both in vitro and in mice (8, 9). PptT catalyzes the Mg²⁺-dependent transfer of 4'-phosphopantetheine (Ppt) from coenzyme A (CoA) onto a conserved serine of the acyl-carrier protein (ACP) domain of fatty acid synthase II, polyketide synthases, and the peptidyl carrier protein domain of nonribosomal peptide synthases (9–11) (Fig. 1A). The free thiol moiety of the phosphopantetheinylated ACP domain allows tethering of substrates and chemical intermediates through a thioester bond, while the flexible Ppt arm facilitates transport of these intermediates to various reaction centers (12). PptT activates enzymes involved in the biosynthesis of structural lipids (mycolic acids) (13) and virulence lipids (siderophores, phthiocerol dimycocerosates, sulfolipids, and phenolic glycolipids) (14, 15).

Multiple drug discovery campaigns have sought small-molecule inhibitors of PptT (9, 10, 16, 17). Amidinouras were identified as whole-cell active, on-target PptT inhibitors by the following criteria: They accumulate unchanged in *Mtb*; are more potent at killing *Mtb* in proportion to the degree to which the expression of PptT is reduced in conditional knockdown (cKD) strains, an effect not seen for 19 other antimycobacterial agents; bind in the PptT active site in cocrystals; are inactive against *Mtb*-bearing certain preservation-of-function point mutations in PptT; and are inactive against *Mtb* with loss-of-function mutations in a newly discovered enzyme, phosphopantetheinyl hydrolase (PptH), that removes Ppt from holo-ACPs (Fig. 1A), augmenting the PptT inhibitory effect of the amidinouras (7, 18, 19). Work on amidinouras continues (20, 21). However, their cardiotoxicity in mice encouraged us to embark on a next HTS against PptT.

¹Department of Microbiology and Immunology, Weill Cornell Medicine, New York, New York 10021, USA. ²Division of Chemical Biology and Medicinal Chemistry, UNC Eshelman School of Pharmacy, University of North Carolina at Chapel Hill, Chapel Hill, NC 27599, USA. ³Department of Biochemistry and Biophysics, Texas Agricultural and Mechanical University, College Station, TX 77843, USA. ⁴Department of Medicine, Weill Cornell Medicine, New York, NY 10021, USA. ⁵Global Alliance for TB Drug Development, New York, NY 10005, USA. ⁶Discovery Sciences, R&D, AstraZeneca, Cambridge CB4 0WG, UK. ⁷Evotec ID (Lyon), SAS 40 Avenue Tony Garnier, Lyon 69001, France. ⁸AMG Consultants Limited, Camburgh House, 27 New Dover Road, Canterbury, Kent, CT1 3DN, UK. ⁹Evonor Consulting Limited, The New Barn, Mill Lane, Eastry, Kent CT13 0JW, UK. ¹⁰Organic Synthesis Core, Memorial Sloan Kettering Cancer Center, New York, NY 10065, USA.

*Corresponding author. Email: nader.fotouhi@tballiance.org (N.F.); jaube@email.unc.edu (J.A.); cnathan@med.cornell.edu (C.N.)

†These authors contributed equally to this work.

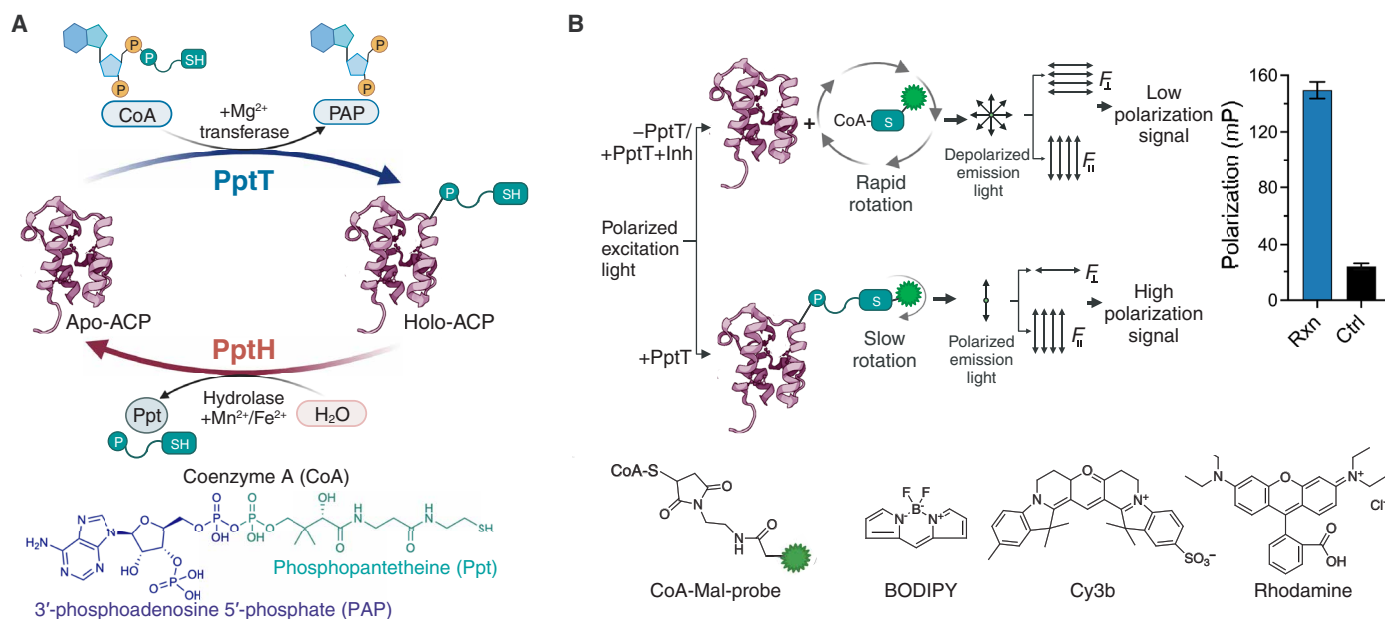


Fig. 1. Optimization of an FP-based activity assay for PptT. (A) Schematic of enzymatic activities catalyzed by PptT and PptH. (B) Representation of the FP-based activity assay in the presence and absence of PptT. Active PptT transfers the fluorophore-labeled Ppt portion of CoA onto the Ser-hydroxyl of another enzyme's ACP domain, resulting in slower rotation of the fluorophore and a higher polarization signal (shown in blue in the bar graph). When PptT is absent or inactive, the fluorophore remains covalently attached to CoA and has a low polarization signal (shown in black in the bar graph). Probes (BODIPY, Cy3b, and rhodamine) were attached to CoA via a Mal-FL-linker. Illustrations were created with BioRender.com.

A drug repurposing library provided the most potent PptT inhibitor yet reported to our knowledge: raltitrexed, an antineoplastic agent that inhibits human thymidylate synthase. Among raltitrexed analogs that inhibited PptT, extensive structure-activity relationship (SAR) studies did not succeed in imparting antimycobacterial activity. Nonetheless, it is instructive to document how *Mtb* defeated our efforts. The target protein markedly changed the shape of its active site when binding the inhibitor; small changes in the inhibitor markedly changed which enzyme the compounds inhibited; and none of the compounds that inhibited PptT escaped extensive catabolism by *Mtb*.

RESULTS

Assay selection, optimization, and HTS

Of various biochemical assays to measure PpTase activity (9, 17, 22, 23), we opted for fluorescence polarization (FP)-based assay introduced for the surfactin synthetase activating protein Sfp, a PpTase from *Bacillus subtilis* (24). We used the N-terminal ACP domain of *Mtb* polyketide synthase 13 (N-ACP PKS13) as a cosubstrate (fig. S1). Since *Mtb* PptT sequesters the Ppt arm of CoA in a hydrophobic pocket (fig. S2A) (10), we adapted the Sfp FP assay for *Mtb* PptT by synthesizing smaller fluorescent CoA derivatives (Fig. 1B and Supplementary methods). After extensive optimization (Supplementary Materials and figs. S2 and S3), the final reaction conditions in a 384-well microplate format (see Materials and Methods) yielded a Z' factor of 0.86 ± 0.06 and a mean signal:background ratio of 2.9. A pilot screen with the 1280-member Library of Pharmacologically Active Compounds (LOPAC) assayed on two different days yielded a Pearson correlation coefficient (r) of 0.7 (fig. S4).

Our screen of 422,740 compounds in the Rockefeller University collection at a concentration of 10 μM identified 0.28% of the compounds as giving $\geq 50\%$ normalized percent inhibition (NPI). From these, we performed confirmation assays on 259 compounds that other screeners had found to be noncytotoxic to the lung fibroblast MRC5 cell line (normalized % cell death of $\leq 30\%$ at 10 μM) and that also had a percent efficiency index (PEI) of 2 to 4 and a quantitative estimate of drug-likeness (QED) of >0.69 (see Materials and Methods). Single-point assays confirmed 65 of these compounds, which were then cherry-picked for concentration-response assays that identified 22 compounds that inhibited 50% of enzymatic activity at concentrations (IC_{50}) $\leq 10 \mu\text{M}$ and achieved a maximum inhibition of $>70\%$ (Fig. 2, A and B). From these, five compounds (RU1, RU2, RU4, RU5, and RU12) were tested with fresh powders and had IC_{50} 's of 65 nM to 7.9 μM (Fig. 1C). RU4, a compound with a tetramethyl pyrrole pyridazine head group, a thiazole core, and a phenyl side chain, had an IC_{50} of 350 nM in the FP-PptT assay and was active against wild-type (WT) *Mtb* with a minimum concentration inhibiting growth by $\geq 90\%$ (MIC_{90}) of 11.5 μM , but it did not gain in potency against the PptT cKD hypomorph (MIC_{90} of 9 μM), indicating that its antimycobacterial activity was likely off-target (Fig. 2C and fig. S5A). RU5, with a thioquinazolinone scaffold, had an IC_{50} of 0.85 μM against PptT. While RU5 lacked inhibitory activity against WT *Mtb*, it was active against the PptT hypomorphic strain (MIC_{90} of 3 μM) (Fig. 2C and fig. S5A), suggesting an on-target effect. Further studies of thioquinazolinones will be reported separately.

RU1 (Raltitrexed), RU2 (cis-C646), and RU12 (hydroxy-dynasore) were identified from a 6143-compound drug-repurposing subset of the library. C646, a 3-methyl-5-oxo pyrazole that inhibits a histone acetyltransferase (25), was the most potent ($\text{IC}_{50} = 3.4 \mu\text{M}$) of five

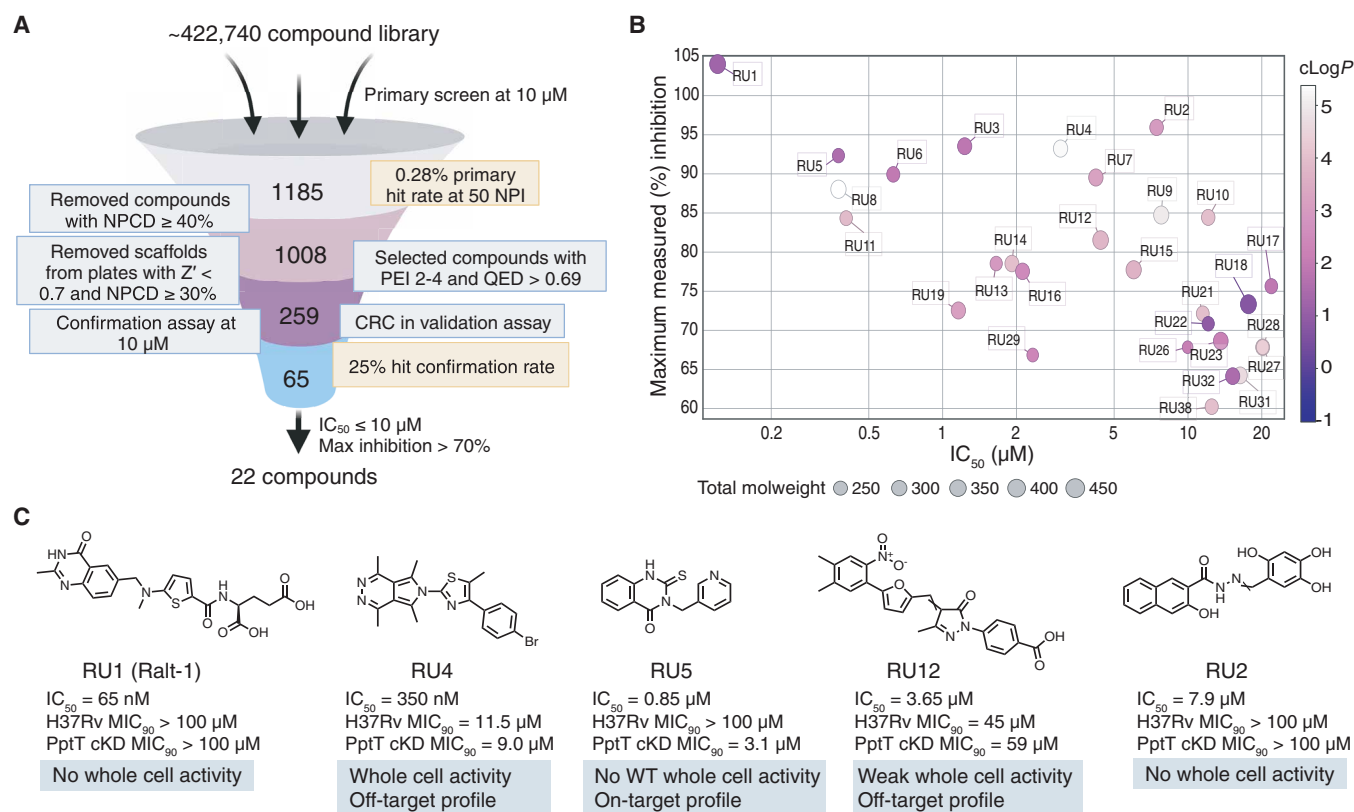


Fig. 2. HTS using FP assay and activity profiles of confirmed hits. (A) HTS funnel showing filtering of PptT active scaffolds. The primary screening assay was performed at 10 μ M concentration using optimized FP-PptT assay. The criteria for selection of scaffolds with drug-like properties were as follows: normalized % cell death (NPCD) of $< 30\%$ for human fibroblast MRC5 cell line; PEI (a ratio of NPI to molecular weight) of two to four and quantitative QED (the sum of weighted functions related to MW, logP, hydrogen bond donors, hydrogen bond acceptors, polar surface area, rotatable bonds, and aromatic rings) of > 0.69 . Schematic was created with BioRender.com. (B) Confirmed hits were cherry-picked for concentration-response (CRC) analysis. XY plot showing IC_{50} (μ M) and maximum measured inhibition (%) in concentration response analysis (in the validation assay) for the confirmed hits with an IC_{50} of < 22 μ M and maximum (%) inhibition of $\geq 60\%$. The circles representing each hit are color coded based on the cLogP (partition coefficient), and their sizes are proportional to the molecular weight. (C) Chemical structures for the validated hits. The corresponding potency against the PptT enzyme, *Mtb* WT strain, and PptT hypomorphic strain (PptT depletion in cKD strain was initiated by withholding of anhydrotetracycline) is listed below the structures. A whole-cell active profile with gain in potency in PptT cKD strain is listed as an on-target profile and with no change in potency for strains with WT and PptT depleted levels is listed as an off-target profile.

analogues that shared the same chemophore (Tanimoto similarity score of ≥ 0.7) (Fig. 2C and fig. S5B). C646 was weakly active against WT H37Rv *Mtb*, with an MIC₉₀ of 45 μ M, but like RU4, showed an off-target whole-cell activity profile (Fig. S5A). The dynamin inhibitor hydroxy-Dynasore (Dyngo-4a) (26), with an IC_{50} of 6.8 μ M, did not inhibit the growth of *Mtb* H37Rv with WT levels of PptT or the cKD strain with reduced levels of the enzyme (Fig. 2C and fig. S5A).

Raltitrexed (hereafter, Ralt-1) is a thymidylate synthase inhibitor marketed as Tomudex for treatment of cancer (27), whose antimitabolite activity depends on polyglutamylation of its carboxylates (28). The IC_{50} of Ralt-1 against rPptT was 730 nM in the FP assay with the stock solution in the screening collection, 65 nM with the resupplied powder, and 250 nM in the BpsA assay (see the Supplementary Materials) with native CoA (Fig. 2C). Ralt-1 showed no activity against H37Rv WT or PptT mutant strains (Fig. 2C and fig. S5A).

We chose to focus on Ralt-1 for two reasons. First, Ralt-1 emerged as the most potent PptT inhibitor identified to date. Second, Ralt-1 achieved a higher maximum inhibition than the amidinourea 8918 (10 μ M) used as the positive control in the HTS. Amidinoureas

inhibit PptT by a noncompetitive mode and achieved no more than 90% inhibition (7). Amidinourea 8918 binds in the CoA (substrate) binding pocket by displacing the Ppt arm into the solution and destabilizes recombinant PptT protein as it is copurified with CoA, as observed by a thermal shift assay (Fig. 3B). In contrast, Ralt-1 afforded a normalized maximum inhibition of $\geq 100\%$ (Fig. 3A) and showed a concentration-dependent stabilization of recombinant PptT with a gain of 15°C in the melting temperature (T_m) at a 1:10 molar ratio of protein to Ralt-1 (Fig. 3B). The concentration-response curve (CRC) for Ralt-1 inhibition of PptT had a Hill slope (h) of 1.6, compared to $h = 1$ for 8918. To explore whether this might indicate tight binding of Ralt-1 to PptT, we preincubated the enzyme-inhibitor complex in equimolar ratio (10 μ M each) and measured recovery of activity after rapid 500-fold dilution (20 nM resulting concentration). PptT recovered activity to the same level as for zero time point addition of 20 nM enzyme and 20 nM Ralt-1 without preincubation (fig. S6). Moreover, IC_{50} s were not affected by the concentration of PptT in the assay (Fig. 3A, inset). These observations suggest that Ralt-1 binding to PptT is readily reversible. Kinetic analysis of recombinant PptT with

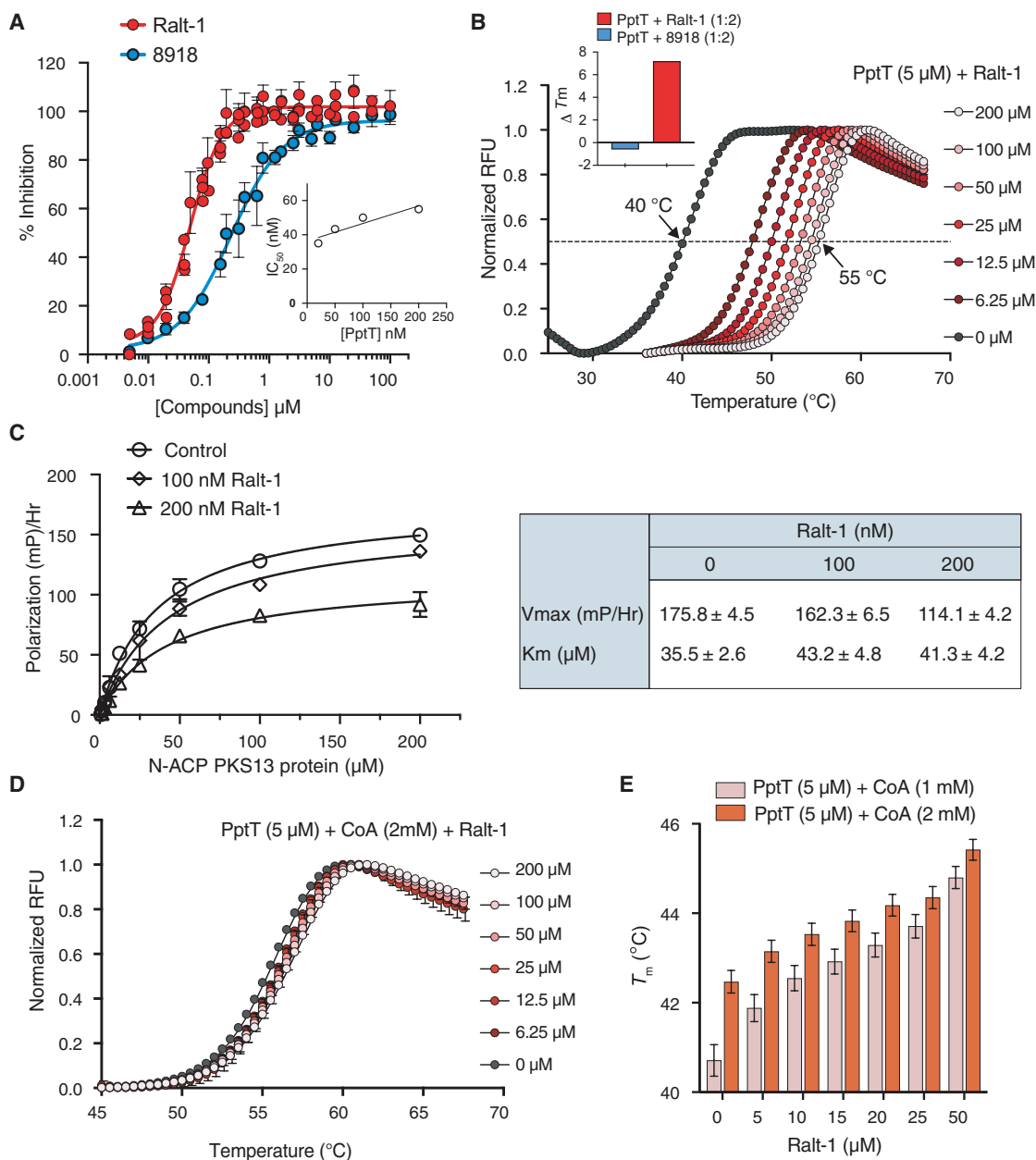


Fig. 3. Inhibition of PptT by Ralt-1. (A) Concentration-response curves for Ralt-1 and amidinouria 8918. Inset showing XY plot of PptT enzyme concentration versus IC_{50} . (B) The melting temperatures (T_m) of recombinant PptT protein were measured in the presence of varying Ralt-1 concentrations (0 to 200 μ M) using a differential scanning fluorimetry (DSF) based thermal shift assay in gel filtration buffer. The T_m was calculated by CFX Maestro software. The inset shows the shift in melting temperatures (ΔT_m) of PptT (10 μ M) upon binding with 1:2 molar ratio of Ralt-1 (20 μ M) or 8918 (20 μ M). (C) Graph showing Michaelis-Menten model curve fits to obtain kinetic parameters in the absence and presence of increasing concentrations (100 nM and 200 nM) of Ralt-1 inhibitor. Apparent reaction velocities in the presence and absence of inhibitor were measured in terms of polarization (mP)/Hr in FP assay with increasing recombinant N-ACP PKS13 domain protein substrate. The table to the right lists the kinetic parameters V_{max} of the reaction and K_m for N-ACP PKS13 protein substrate. (D and E) T_m of CoA-preincubated PptT protein upon addition of Ralt-1 (D) DSF profile in the gel filtration buffer and (E) bar graph of T_m in Hepes buffer condition.

the N-ACP PKS13 substrate revealed a decline in apparent maximum rate of reaction (V_{max}) with increasing Ralt-1 concentrations without affecting the apparent Michaelis constant for the ACP substrate (Fig. 3C), suggesting a noncompetitive mode of inhibition with respect to the ACP substrate.

We questioned whether Ralt-1's lack of whole-cell activity could be attributed to an inability to compete with CoA at high concentrations,

such as might be found within *Mtb*. However, when we preincubated PptT (5 μ M) with 1 mM or 2 mM CoA, Ralt-1 fortified PptT against heat denaturation in the buffer used for gel filtration (Fig. 3D). The impact was minor in buffer with 20 mM Hepes (pH 7.5), 200 mM NaCl, 20 mM $MgCl_2$, and 5% glycerol and the stabilizing agents 50 mM arginine and 50 mM glutamate but became pronounced when the stabilizing agents were omitted (ΔT_m of 4°C and 3°C for 1 and 2 mM

CoA-preincubated PptT, respectively, in the presence of 50 μ M Ralt-1) (Fig. 3E). In the gel filtration buffer, CoA-bound PptT displayed a T_m of $\sim 56^\circ\text{C}$, while absent the stabilizing components in the buffer, CoA-bound PptT had T_m of $\sim 40^\circ\text{C}$, allowing Ralt-1 to impart a greater degree of stabilization on its own (Fig. 3, D and E). These results provide strong evidence that Ralt-1 binds PptT and militate against CoA outcompeting Ralt-1 for binding to PptT within *Mth*. The former conclusion was reinforced by isothermal titration calorimetry in the HEPES-based buffer conditions with CoA-saturated PptT as the macromolecule and Ralt-1 as titrant. At a stoichiometry (n) of 1, the dissociation constant (K_d) for binding was 290 ± 29 nM, with changes in both enthalpy and entropy contributing binding free energy (fig. S7). These indications of stronger binding and a different mechanism of action for Ralt-1 than for amidinouras invited closer study, including a structural analysis.

Cocrystal structure

A crystal structure of a Ralt-1–PptT complex was indexed and scaled in the $P4_12_12$ space group, with nine molecules of PptT in the asymmetric unit, at 2.4-Å resolution (data collection and refinement statistics are in table S2). While the ligand density was strong and obvious for all chains, three of the nine protein chains had much poorer density, particularly chain F. Multiple attempts to rebuild and use of a noncrystallographic symmetry aid and correction during refinement did not improve the definition of these chains. Accordingly, we removed a large part of chain F and some parts of chains G–I from the final deposited model. While this negatively affected the resultant refinement R factors, the five chains (A to E) with good density represent the structure well enough for the purposes of this study. There was a strong electron density for the ligand observed in the positive Fo–Fc difference electron density map on every chain, allowing for unambiguous placement of the Ralt-1 molecule. Compared to a previously solved complex with an amidinouras inhibitor [Protein Data Bank (PDB) ID 6CT5] (7) and a CoA-bound structure (PDB ID 4QJK) (10), there are changes to the PptT active site (Fig. 4, A and B). The amidinouras inhibitor replaces the Ppt moiety of CoA but leaves the phosphoadenosine phosphate of CoA visible in the electron density, along with two Mg^{2+} ions, one of which displaces the side chain of His93 from the position it occupies in the CoA-bound structure (7). In contrast, Ralt-1 completely displaces CoA and reshapes part of the active site. The quinazolinone ring of Ralt-1 forces the side chain of Tyr¹⁶⁰ to flip, creating a pocket for stacking the quinazolinone between the side chains of Tyr¹⁶⁰ and Trp¹⁷⁰, with the indole of Trp¹⁷⁰ shifting in the same plane by $\sim 20^\circ$ compared to the CoA-bound structure. Two H-bonds strengthen the interaction in this pocket: between the quinazolinone nitrogen and the backbone carbonyl of Leu¹⁷¹ (N3 to O, 2.9 Å) and between the quinazolinone carbonyl group and the backbone NH of Leu¹⁷¹ (O4 to N, 2.78 Å). The thiophene of the inhibitor binds near the position of the CoA adenine. The carbonyl group of the Ralt-1 amide group H-bonds through water with the Ser⁹⁰ side chain (O1 to HOH to OG at 2.72 and 3.0 Å) and to the backbone NH of Leu⁹¹ (O1 to HOH to N, 2.72 and 2.56 Å). The two carboxylates of the inhibitor reach polar pockets of the active site that accommodate phosphates of CoA. One carboxylate engages in an H-bond with His⁹³ (O3 to ND1, 2.62 Å), pulling it closer into the active site compared to the CoA-bound structure, into a position overlapping with the Mg^{2+} ion in the amidinouras-bound structure (Fig. 4, A and B). The same oxygen (O3) of the inhibitor H-bonds with another carboxylate of Ralt-1 through a water molecule (O3 to HOH to O5 at 2.51 and 2.82 Å).

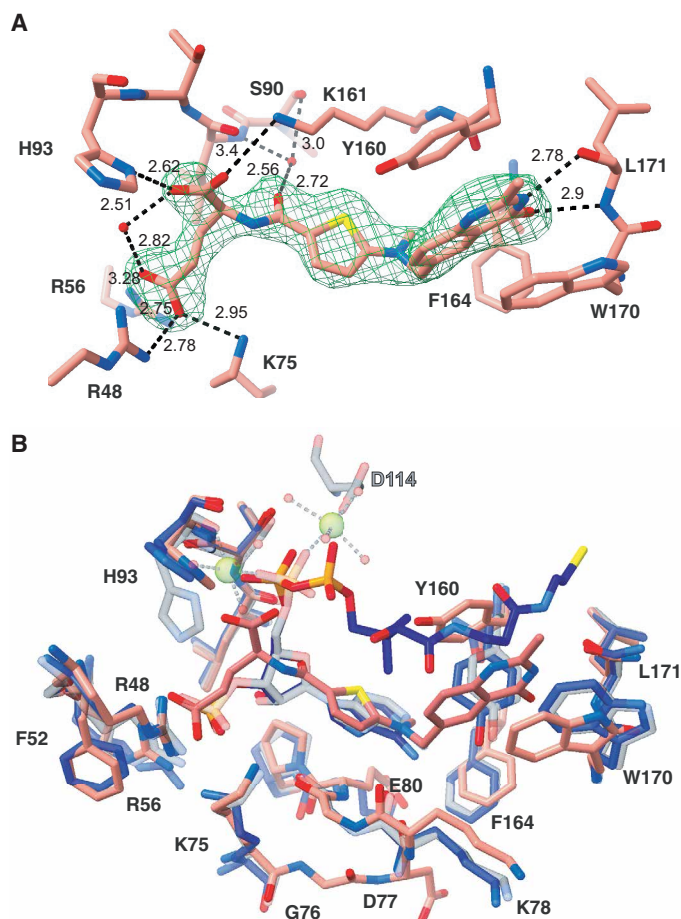


Fig. 4. Crystal structure of PptT-Ralt-1 binary complex. (A) Ralt-1 bound in the active site of PptT. Hydrogen bonds are shown as dashed lines with distances in angstrom noted. Polder omit map Fo–Fc electron difference map density is displayed as a green mesh with 4 sigma cutoff level (B) Superposition of PptT bound to Ralt-1 (salmon carbons structure), CoA (blue carbons, 4U89), and CoA-amidinouras 8918 (gray carbons, 6CT5). Protein residues with notable changes in position upon Ralt-1 binding are shown and labeled in black. Gray labeled residue D114 and green spheres representing Mg atoms are from the 8918–CoA–PptT complex (PDB ID 6CT5) structure. The 8918 aligns with ppt arm of CoA and overlays onto the quinazolinone head group of Ralt-1; therefore, it has been omitted for structural representation here. Representative images were generated using ChimeraX.

The other oxygen of this carboxylate bonds with the Lys¹⁶¹ side chain (O4 to NZ, 3.4 Å). The carboxylate of the glutamate moiety of Ralt-1 interacts with the side chains of Arg⁴⁸, Arg⁵⁶, and Lys⁷⁵ (Fig. 4, A and B). These three residues interact with the 3-phosphate group of CoA in a substrate-bound structure (PDB ID 4QJK) (Fig. 4B).

SAR for improved potency

Ralt-1 was discovered (29, 30) by Imperial Chemical Industries PLC, Pharmaceutical Division, now part of AstraZeneca, as a selective inhibitor of thymidylate synthase (31). To seek analogs with greater inhibitory potency for PptT, we turned to the collection that AstraZeneca compiled in the course of developing Ralt-1 and screened 721 analogs that have an extended connectivity fingerprint, up to four bonds (ECFP4) similarity to Ralt-1 of >0.7 . Of these, 332 inhibited

PptT in the FP assay by >30% at 30 μ M. The analysis presented here is based on assays with the 649 compounds that continued to show >85% purity after many years of storage.

Ralt-1-like diacids were more potent in the FP assay than monoacid and neutral analogs (fig. S8). Of the diacid analogs, 17 were more potent than Ralt-1 (AZ1), the lowest IC₅₀ being 18 nM (fig. S8 and table S4), a ~3-fold improvement compared to Ralt-1. SAR analysis of these 17 Ralt analogs revealed minor substitutions to the linker and thiophene core that can lead to increased potency or are permissive for the inhibitory activity (Fig. 5A and table S4). Thiazole or phenyl replacing the thiophene core results in equivalent potency. The most potent compound, AZ6, bears an allyl substituent on the methyl-bearing nitrogen of Ralt-1 (Fig. 5A and table S4). The increased

potency of AZ6 may result from the increased length of the alkyl group protruding into the hydrophobic pocket occupied by the methyl group of Ralt-1. This is supported by the crystal structure, which suggests that longer alkyl groups may be preferred due to their ~109° angle in the side chain that allows the other atoms of the alkyl chain to better fit in the narrow hydrophobic channel. Among analogs of the thiazole core, an allyl (AZ8) or propynyl (AZ9) substitution resulted in better potency than ethyl (AZ7) substitution (Fig. 5A and table S4). Other potency enhancements arose from addition of a fluorine or a hydroxyl to the phenyl core, as in AZ23 or AZ24, respectively (Fig. 5A and table S4).

However, the diacid raltitrexed analogs were inactive in the whole-cell activity assay against WT *Mtb* (MIC₅₀ > 15 μ M). Therefore,

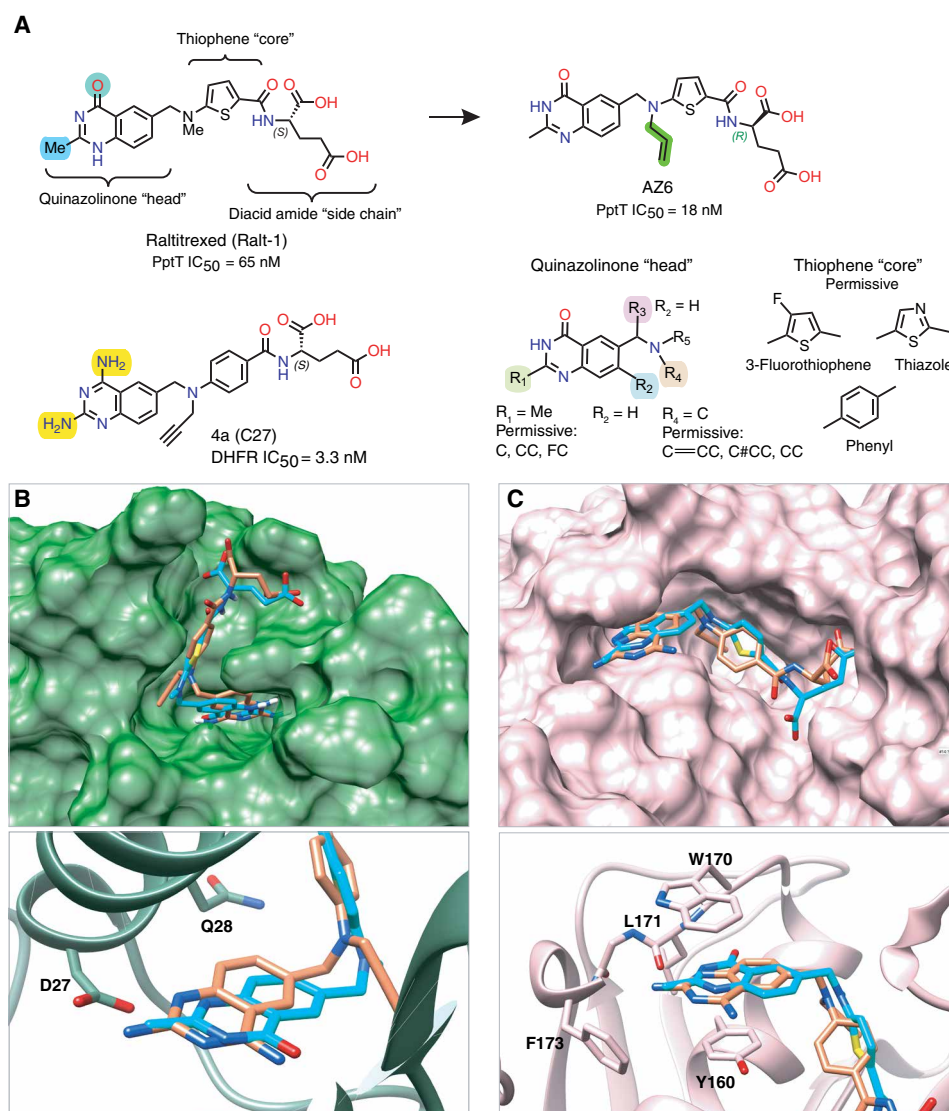


Fig. 5. Ralt-1 and 4a binding at active sites of DHFR and PptT. (A) Chemical structures of Ralt-1, the most potent Ralt-1 analog (AZ6) and 4a. The bottom right presents the SAR analysis of permissive chemical moieties at Ralt-quinazolinone head group and thiophene core to gain potency against PptT. (B) Surface view of DHFR active site structure (green; energy minimized protein backbone of structure of PDB ID 6DDW) with docked poses of Ralt-1 and 4a, shown as sticks in cyan and orange, respectively. (C) Surface view of PptT active site structure (pink; energy minimized protein backbone of PptT-Ralt-1 complex) with docked poses of Ralt-1 and 4a, shown as sticks in cyan and orange, respectively. Three-dimensional molecular docking images in the bottom show protein structures in ribbon and surrounding amino acid residues in stick. Representative images were generated using Chimera.

monoacidic and neutral Ralt-1 analogs with high IC_{50} 's in the FP assay (1 to 6 μ M) but with physical properties amenable to bacterial cell permeability were screened in the whole-cell assay at concentrations up to 100 μ M. Four compounds with good Caco-2 permeability and moderate efflux ratios indicative of good intrinsic permeability had modest whole-cell activity but that activity was off-target (table S5). Conversely, the most potent whole-cell actives (MIC_{90} 's 4 to 10 μ M) were basic analogs that were inactive in the PptT FP assay, again indicating an off-target mode of action.

SAR for whole-cell activity

In an effort to improve whole-cell activity, we considered three sections of Ralt-1: the quinazolinone "head," the thiophene "core," and the di-acid amide "side chain" (Fig. 5A). As we learned from the co-crystal structure and the SAR analysis with AstraZeneca compounds, the quinazolinone head interaction strengthens the binding of Ralt-1 in the reshaped binding pocket in PptT, likely contributing to the potency of Ralt-1 and many of its analogs. Although an allyl-bearing N connecting the thiophene core to the quinazolinone head improves binding, the thiophene core posed a threat due to its potential to form reactive metabolites (32). The di-acids of the side chain were additional liabilities, as they are the sites of polyglutamylation in human cells, which equips raltitrexed to inhibit thymidylate synthase (31). Moreover, they could plausibly be responsible for poor intrabacterial uptake. With these concerns in mind, our goals were to maintain the potent PptT binding activity of Ralt-1 while gaining whole-cell activity against *Mtb*.

The SAR campaign for whole-cell activity began with a simple phenyl replacement of the thiophene core (**3a**, Table 1). This compound maintained the sub-100 nM potency of Ralt-1, without the structural alert of the thiophene. Further analogs were synthesized with either thiophene or phenyl cores, based on synthetic convenience.

To promote uptake into the pathogen, a classic prodrug strategy for antibacterials is to esterify polar functional groups and rely on intrabacterial esterases to regenerate the parent compound (33). To probe changes in Ralt-1's di-acid side chain, we first made the *R* enantiomer of Ralt-1, compound **2a**. Its IC_{50} of 73 nM indicated that the absolute configuration of the parent molecule is not crucial. Next, we masked the acids with alkyl esters (**2b-d**, **3b**) and prepared monoacids (**2e-f**). Of those analogs, only **2f** retained comparable potency to Ralt-1, but it still lacked whole-cell activity against *Mtb* H37Rv ($MIC_{90} > 100 \mu$ M). Next, we prepared acid and ester bioisosteres predicted to have greater lipophilicity (logD 7.4) and greater permeability (logP_{app}) based on Lassalas *et al.* (34). These included tetrazoles (**2g-l**), sulfonamides (**2m-n**, **3c**, and **3h**), a phenol-substituted sulfoxide (**2o**), and a thiadiazol-5(4*H*)-one (**2p**). Some of these analogs retained the in vitro potency of Ralt-1, but none had whole-cell activity against *Mtb*.

In addition to bioisosteres, we synthesized heterocycles with hydrogen bond donors, such as pyridine **2r**, indazoles **2t** and **3d**, imidazoline dione **2q**, and pyrimidine dione **2v**. Cyclizing the di-acid into five- or six-membered rings as in **3e-g** led to analogs that retained some of the binding potency of **1**. Simpler heterocyclic replacements of the quinazolinone head afforded other approaches to increased lipophilicity (table S3), but none of these analogs inhibited PptT with an $IC_{50} < 50 \mu$ M.

Of the 105 compounds that we synthesized in an effort to gain whole-cell activity, only **2d**, **2t**, and **3d-e** showed both PptT inhibitory

activity and whole-cell activity, but the whole-cell activity was weak; the most potent compound was the cyclized di-acid **3e** with an MIC_{90} of 34.8 μ M against the WT H37Rv strain (Table 2). Moreover, the whole-cell activity of those compounds did not appear to be on-target, as the *pptT* cKD hypomorph strain showed only a marginal increase in susceptibility.

Ligand selectivity

Drug development campaigns have been pursued against the dihydrofolate reductases (DHFRs) of *Mtb* (35), leading to the identification of two *Mtb* DHFR inhibitors with a 2,4-diamino-quinazoline head group (**C27** and **C29**) (36). The notable similarity of these compounds to Ralt-1 intrigued us, given that DHFR and PptT do not share overall structural similarity, a functional domain or a conserved motif for ligand binding. Adding further interest, **C27** was reported to be active against WT *Mtb*, with an MIC of $\sim 5 \mu$ M (36), despite having a diacid amide tail. We synthesized **C27** (**4a**) and **C29** (**4b**) and confirmed their inhibition of recombinant *Mtb* DHFR and their whole-cell activity (Table 3). Despite their resemblance to Ralt-1, neither compound inhibited PptT in vitro or in *Mtb* (Table 3). Like **2d**, the diethyl ester analog of **C27** (**4c**) showed reduced inhibitory activity for DHFR, but the H37Rv WT strain was more susceptible to **4c** than to **4a**. Both *S*- and *R*-methyl esters of **C29** (**4d** and **4e**) had comparable activity to **C27**. These ester analogs also lacked activity against PptT (Table 3).

Ralt-1 had an IC_{50} against *Mtb* DHFR of 8.5 μ M, while the IC_{50} of **4a** for *Mtb* DHFR was 3.3 nM. A comparison of Ralt analogs acting as DHFR inhibitors (**4a** analogs) and those acting as PptT inhibitors (Ralt-1 analogs) suggested that DHFR inhibitors share a 2,4-diamino-quinazoline ring, while PptT inhibitors have a 2-methyl-4-oxo-quinazoline (quinazolinone) ring (Fig. 5A). Binding of Ralt-1 to the PptT ligand-binding site flipped the conformation of Tyr¹⁶⁰, creating a binding pocket for its head group, while a compound with a 4-oxo substituted amino group may bind in inverse orientation in the *Mtb* DHFR pocket, weakening its affinity (35). Docking analysis of **4a** at the substrate-binding site of DHFR suggested that the compound's 2-amino moiety fits in a hydrophilic pocket bounded by Asp²⁷, Gln²⁸, and Thr¹¹³, contributing to a docking score of $-9.4 \text{ kcal mol}^{-1}$ (Fig. 5B). Asp²⁷ is a critical residue in DHFR that restrains the substrate in a conformation favorable for hydride transfer (37). The 2-amino moiety of the **4a** quinazoline is stabilized by an H-bond interaction with Asp²⁷ (Fig. 5B). In contrast, Ralt-1, with its hydrophobic 2-methyl quinazolinone, docks away from the **4a** binding position (docking score of $-8.8 \text{ kcal mol}^{-1}$) (Fig. 5B).

At the PptT reshaped active site, a neutral form of **4a** docks with a score of $-10.37 \text{ kcal mol}^{-1}$, compared to Ralt-1's score of $-10 \text{ kcal mol}^{-1}$ (Fig. 5C). Given that **4a** is larger than Ralt-1, the ligand efficiency for **4a** is less (0.296) than that of Ralt-1 (0.322), suggesting that Ralt-1 has better binding parameters (38, 39). However, no PptT inhibition was observed with **4a** ($IC_{50} > 25 \mu$ M) (Table 3), indicating that **4a** binding is not sufficient for enzyme inhibition.

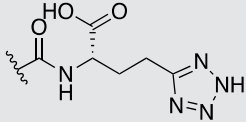
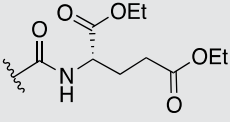
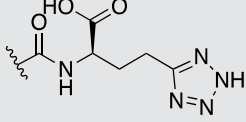
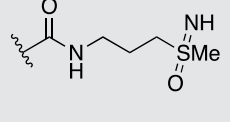
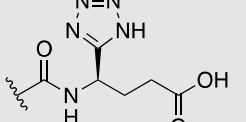
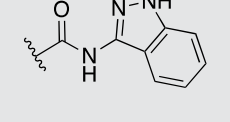
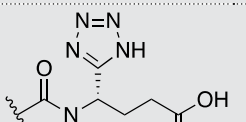
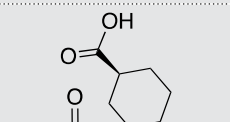
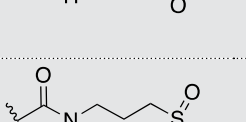
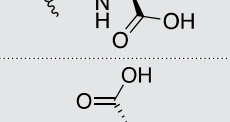
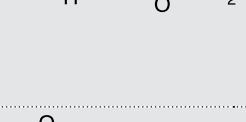
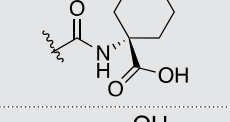
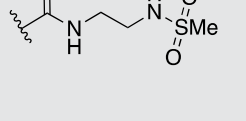
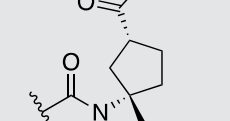
To further explore how modification of the quinazolinone moiety provides specificity for PptT inhibition, we obtained additional raltitrexed analogs from Merck & Co. Inc., Rahway, NJ, USA, **4g-h** (Table 3). The absence of the 2-methyl substituent on the quinazolinone or its replacement by a 2-amino group decreased potency against PptT by ~ 6 -fold, while substitution of 4-oxo by 4-amino on the quinazoline drove the IC_{50} over 100 μ M (Table 3), suggesting that the

Table 1. Selected analogs.							
Thiophene core				ID	R	IC ₅₀ * PptT (μM)	h [†]
				2p		0.08	1.4
ID	R	IC ₅₀ * PptT (μM)	h [†]	2q		2.69	0.7
Ralt-1		0.07	1.5	2r		2.31	0.9
2a		0.07	2.0	2s		0.33	1.1
2b		12.5	0.7	2t		1.0	1.0
2c		7.5	0.7	2u		2.03	1.0
2d		1.19	0.8	2v		0.53	1.0
2e		0.21	1.1	Phenyl core			
2f		0.10	1.5				
2g		0.20	1.2	ID	R	IC ₅₀ * PptT (μM)	h [†]
2h		1.01	1.2	3a		0.09	1.4

(Continued)

Downloaded from https://www.science.org on April 11, 2025

(Continued)

2i		0.18	1.3	3b		>50	–
2j		0.08	1.7	3c		33.9	–
2k		0.04	2.4	3d		1.36	1.1
2l		0.07	1.8	3e[‡]		0.44	0.9
2m		0.76	1.0	3f[‡]		0.29	1.0
2n		1.13	1.0	3g[‡]		0.06	1.4
2o		0.22	1.1	3h		24	–

*IC₅₀ determined via FP assay at 100 nM PptT enzyme concentration. [†]*h* = Hill slope. [‡]The stereostructures of **3e–3g** are drawn based on literature precedent for their synthesis but were not rigorously determined (see the Supplementary Materials).

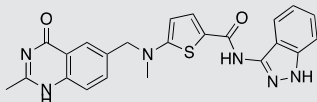
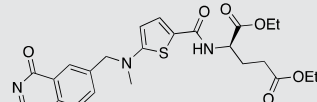
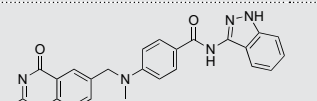
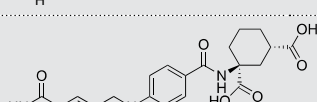
4-oxo quinazolinone head group H-bond interaction with PptT Leu¹⁷¹ backbone is critical for its binding. Collectively, these results illustrate that minor alterations to the parent structure on the quinazoline (2,4-diamino substitution to 2-methyl-4-oxo) can have a remarkable effect on which of these unrelated enzymes is inhibited.

Intrabacterial pharmacokinetics

After testing 826 analogs of Ralt-1, we had not learned why the potent PptT inhibitors among them all failed to strongly inhibit the

growth of *Mtb*. To solve this mystery, we turned to an liquid chromatography–mass spectrometry (LC-MS)–based metabolomics platform for *Mtb* in which compounds of interest are recognizable as analytes from the appearance of unique mass/charge ratio species in bacterial lysates following exposure of the bacteria to the compounds (7, 40). By studying lysates of bacteria on a filter floating on a fluid reservoir to which the compound of interest (10 μM) has been added, the proportion of compound associated with the bacteria can be compared to that remaining in the reservoir, and modified

Table 2. Raltitrexed analogs showing anti-*Mtb* activity.

ID	Structure	IC ₅₀ PptT (μM) [†]	MIC ₉₀ (μM)*			ΔPptH
			H37Rv	PptT KD -ATc	PptT KD +ATc	
2t		1.04	67.6 [‡]	39.4 [‡]	50.5 [‡]	63.2 [‡]
2d		1.19	80.3	43.7	75.7	>100
3d		1.36	32.2 [‡]	97.6 [‡]	50.8 [‡]	96.5 [‡]
3e[§]		0.44	34.8	29.0	26.4	27.0

*MIC₉₀ for inhibition of *Mtb* growth in vitro for H37Rv (WT *Mtb*), an *Mtb* strain in which PptT is knocked down by SspB-controlled proteolysis of a DAS-tagged PptT allele in the absence of anhydrotetracycline (ATc) or inducibly relieved from knockdown in the presence of ATc, and a *pptH* KO strain of *Mtb*. [†]IC₅₀ determined via fluorescence polarization assay at 100 nM PptT enzyme concentration. [‡]MIC₅₀ for inhibition of *Mtb* growth in vitro for H37Rv (WT *Mtb*), an *Mtb* strain in which PptT is knocked down by SspB-controlled proteolysis of a DAS-tagged PptT allele in the absence of anhydrotetracycline (ATc) or inducibly relieved from knockdown in the presence of ATc, and a *pptH* KO strain of *Mtb*. [§]Stereostructure assignment tentative.

forms of the compound of interest can be identified in both compartments (see Materials and Methods). We selected five raltitrexed analogs as test agents that at least showed weak whole-cell activity when compared to parent Ralt-1 (Fig. 6A and table S6). For Ralt-1, $1.2 \pm 0.1\%$ of the drug was recovered from the cells. In comparison to the di-acid, $74.6 \pm 6.7\%$ of the *R*-configured diethyl ester analog (**2d**) was taken up, and of this proportion, ~93.6% was metabolized, but only a small fraction remained within the cells as the di-acidic parent and the remaining products were unidentified. After treatment with **2d**, parent Ralt-1 was found both in lysates and in the extracellular reservoir which collectively accounted for 11.9% of the proportion of the diester that was metabolized. No Ralt-1 was found on the filter or in the reservoir in cultures lacking *Mtb*, which suggests that *Mtb* effluxes free Ralt-1. We conclude that the diester was readily taken up and extensively metabolized, for the most part into products other than Ralt-1; of the Ralt-1 formed and not further metabolized, most was pumped back out into the extrabacterial space. Further analysis on biotransformation patterns in samples treated with 100 μM **2d** suggested a progressive loss of the ethyl esters and a methyl group, indicated by different combinations of 14 and 28 mass unit losses of compounds that eluted at increasingly later times, consistent with them becoming more polar (Fig. 6B). LC–tandem mass spectrometry (MS/MS) analysis revealed demethylation, most likely at the tertiary amine connecting the quinazolinone ring and the thiophene core (fig. S9). **2s**, an analog with an intact γ -carboxylic acid, was also extensively taken up ($55.4 \pm 7.4\%$); of that proportion, $14 \pm 3\%$ remained unmodified, while 86% was metabolized to unidentified products. Similar uptake and metabolism profiles were observed for **2r** and **2t**, which lacked both acid moieties.

Overall, the analyses of intrabacterial pharmacokinetics indicated that the Ralt analogs lacking acid(s) were taken up to an extent $\geq 50\%$, but their extensive biotransformation was the primary factor that prevented them from exerting intrabacterial on-target activity.

DISCUSSION

Several criteria serve to prioritize enzymes in a bacterial pathogen as targets for the intensive effort required to develop an anti-infective agent. PptT meets the first criterion for a target for a drug against *Mtb*: its catalysis of the first step in the synthesis of complex lipids that *Mtb* uses for its cell wall and virulence factors makes PptT essential for *Mtb*'s survival, not only under standard growth conditions in vitro but also in a mouse model of tuberculosis (9). PptT was not ranked as a highly vulnerable target in *Mtb* (41), but the ranking was based on studies of *Mtb* in vitro. PptT appears to be a vulnerable target in vivo, in that growth of *Mtb* in mice was prevented by a compound that does not inhibit the enzyme completely in vitro (7). On the basis of PptT's in vivo essentiality and vulnerability, we set out to seek inhibitors with greater potency and better pharmacologic properties than amidino-ureas. We opted for an FP-based, direct, continuous enzyme assay and optimized the reaction conditions to support HTS.

We identified raltitrexed (Ralt-1) as a ~50 nM reversible PptT inhibitor with two liabilities: anti-proliferative activity against human cells and a lack of whole-cell activity against *Mtb*. We embarked on an SAR campaign to systematically modify each of raltitrexed's constituent chemophores—a quinazolinone linked through a thiophene to dicarboxylic acids—with the intent of overcoming both problems. However, after studying more than 800 analogs, we did not find one

Table 3. Activity of raltitrexed analogs showing different target selectivity.							
ID	Structure	IC ₅₀ [†] DHFR (nM)	IC ₅₀ [‡] PptT (μM)	MIC ₉₀ (μM)*			
				H37Rv	PptT KD –ATC	PptT KD +ATC	ΔPptH
Ralt-1		8.5 × 10 ³	0.065 [§]	>100	>100	>100	>100
4a (C27)		3.3	>25	5.0	3.2	3.7	4.8
4b (C29)		23.1	>25	0.07	<0.2	<0.2	<0.2
4c		200	>25	0.03	<0.2	<0.1	<0.1
4d		83.3	>25	<0.1	<0.1	<0.1	<0.1
4e		38.4	>25	<0.1	<0.1	<0.1	<0.1
4f		–	0.05 [§]	>100	>100	>100	>100
4g		–	0.33	>100	>100	>100	>100
4h		–	0.27	–	37.4	76.7	–
*MIC ₉₀ for inhibition of <i>Mtb</i> growth in vitro for H37Rv (WT <i>Mtb</i>), an <i>Mtb</i> strain in which PptT is knocked down by SspB-controlled proteolysis of a DAS-tagged PptT allele in the absence of anhydrotetracycline (ATC) or inducibly relieved from knockdown in the presence of ATC and a <i>pptH</i> KO strain of <i>Mtb</i> . †IC ₅₀ determined at 200 nM DHFR enzyme concentration. Trimetrexate, used as the positive control, fits to IC ₅₀ of 28 nM in the same assay conditions. ‡IC ₅₀ determined via fluorescence polarization assay at 100 nM PptT enzyme concentration. §Hill slope (<i>h</i>) ~ 1.5.							

that both potently inhibits PptT and inhibits the growth of *Mtb* by virtue of inhibiting PptT. We drew three lessons from this experience that may help others seeking to develop anti-infective agents.

First, one inhibitor that binds an enzyme’s active site can markedly change the conformation of the active site, although another inhibitor that binds to the same site does not. This has been observed with other enzymes but has rarely been reported for targets of antibiotics and

had not been reported for PptT. As a recombinant protein, PptT copurifies from a host cell with CoA bound to it, and there is no experimentally solved apo structure (7). However, the AlphaFold prediction for the apo state of PptT (AF-A0A654U4E2-F1; not shown) closely replicates the CoA-bound, experimentally determined structure (PDB ID 4QJK), including the positions of the side chains of residues that surround the active site. The Ralt-1–PptT complex structure

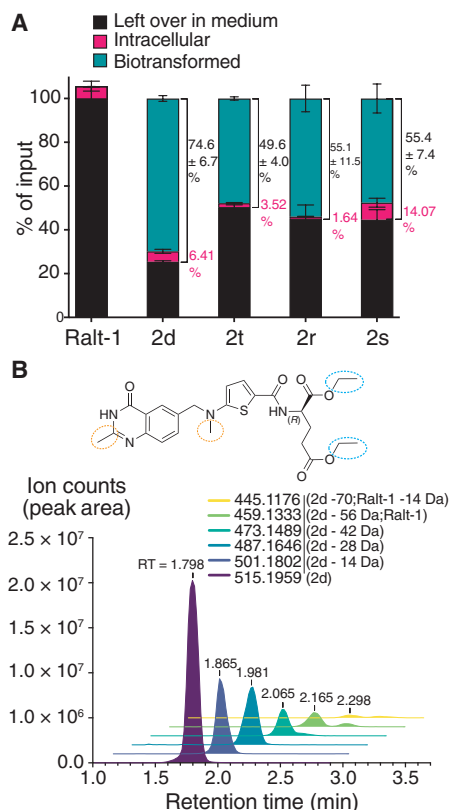


Fig. 6. Intrabacterial pharmacokinetic analysis of Ralt-1 and ester analogs. (A) Mats of *Mtb* grown on filters were exposed to 10 μ M of test compounds for 24 hours. The contents of the reservoir and of the filter were individually subjected to organic extraction and LC-MS analysis, along with samples from wells whose filters carried no *Mtb*. The quantity of test agent added to the reservoir is set as 100% input. Y axis on the bar graph represents % of input test compound left in medium (in black), intracellular remaining as parent (in pink), and biotransformed (in green) whether found in the cells or in the medium. (B) Biotransformation products of **2d**. *Mtb* was treated with 100 μ M **2d** and subjected to metabolic profiling to identify biotransformation products. Data shown are extracted from Agilent MassHunter Qualitative Analysis Navigator software, representing chromatographic profiles of **2d** metabolites from the same lysates. Losses of 28 and 56 Da represent losses of mono and di-ethyl ester(s), respectively, represented in blue dotted circles in the chemical scaffold above the graphs. A loss of 14 Da is predicted to indicate demethylation at either the 4-methyl of the quinazolinone or the tertiary amine methyl, both highlighted with an orange dotted circle in the chemical scaffold above the graphs.

revealed a complete displacement of CoA from the active site and compound-induced conformational changes of Arg⁴⁸, Arg⁵⁶, Lys⁷⁵, His⁹³, Glu¹¹⁶, Trp¹⁷⁰, and Lys¹⁶¹ residues. Among these, relocation of Tyr¹⁶⁰ is particularly impactful in creating an active site cavity between Tyr¹⁶⁰ and Trp¹⁷⁰ that differs in shape and properties from that observed in the model apo structure (AF-A0A654U4E2-F1), CoA-bound structure (PDB ID 4QJK) or inhibitor-bound structure (PDB ID 6CT5) of *Mtb* PptT. Using any of the non-Ralt-1-bound conformations of the active site of PptT in molecular docking or virtual screening would not have allowed us to find the experimentally observed Ralt-1-bound state of PptT. As computational methods are used increasingly in antibiotic discovery, our observations underscore that it is a potentially disqualifying limitation to interrogate only one

known or predicted active site conformation, because ligand binding can reshape a protein binding site.

On the basis of the PptT structure in its Ralt-1-binding form, we used a flexible Vina docking interface to evaluate binding of ideated compounds before their synthesis. For example, exploring chemical space around the diacids showed critical interactions with charged amino acids Arg⁴⁸, Arg⁵⁶, Lys⁷⁵, His⁹³, and Glu¹¹⁶. However, multiple bioisosteres synthesized on this basis and potent against PptT in vitro lacked activity against *Mtb* that could be attributed to inhibition of PptT. Vina docking did allow us to identify a hydrophobic pocket that was occupied by the methyl group on the linker nitrogen atom and predicted that longer substituents in this position could be beneficial. This was confirmed by the PptT inhibition assay, in the case of the propenyl substituent of AZ6 and the propyne of **4f**. However, these changes did not provide favorable results when tested against *Mtb* cells.

This brought us to a second lesson: that minor chemical changes introduced in an SAR campaign that confer a desired result—in this case, increased whole-cell activity—can do so by changing which enzyme is inhibited. PptT shows specificity for the 4-oxo moiety in the quinazolinone ring of raltitrexeds (Table 3), a moiety that is replaced by a 4-amino group in DHFR inhibitors. A 2-amino moiety in the pteridine ring (as in methotrexate) or quinazoline ring (as in **4a**) is crucial for potency of DHFR inhibitors, while a 2-amino moiety can be accommodated at the PptT binding site. A hybrid with a 2-amino, 4-oxo quinazoline ring could be predicted to act as a dual inhibitor of PptT and DHFR. Such polypharmacology would be welcome but would only be useful if a way could be found to overcome extensive metabolism of such a compound by *Mtb*. This underscores the importance of examining both target inhibition and mechanism of growth inhibition in a drug discovery campaign rather than assuming that the former explains the latter.

Comparison of raltitrexeds as *Mtb* PptT inhibitors and methotrexate analogs as *Mtb* DHFR inhibitors brought us to the third lesson—the critical role of monitoring intrabacterial compound accumulation, transformation, and excretion in interpreting the SAR of anti-infective agents. That the lack of whole-cell activity of Ralt-1 might be due to poor uptake related to its carboxylates was a reasonable hypothesis, based on experience with methotrexate and its esters (42). Methotrexate is a more potent inhibitor of *Mtb* DHFR than its esters but lacks whole-cell activity against *Mtb* (MIC₉₀ > 100 mM), while its dimethyl and diethyl esters have MIC₉₀'s of 30 to 50 nM (42). Metabolite analysis showed that the di-esters are hydrolyzed inside *Mtb* to methotrexate or methotrexate monoester (42). However, a quinazoline ring-containing methotrexate analog with diacids (**C27** and **4a**) was active against *Mtb* (36). We synthesized **4a**, its *tert*-butyl ester (**C29**; **4b**) and its diethyl ester (**4c**). **4c** had a ~66-fold higher IC₅₀ on *Mtb* DHFR than **4a** but ~180-fold lower MIC₉₀ against WT *Mtb* H37Rv (Table 3). We concluded that the diethyl ester, **4a**, acts as a prodrug that is hydrolyzed by *Mtb* esterases to release the parent acid or monoester derivatives. To compare with the functional groups of **4a**, we synthesized a Ralt-1 analog with a phenyl core and an acetylene linker (**4f**). The compound's potency against PptT was comparable to that of Ralt-1, but it still lacked whole-cell activity (Table 3). Every ester analog of **4f** we synthesized (**7a-c**) was inactive or only weakly active at inhibiting growth of *Mtb* (table S7).

Intrabacterial pharmacokinetic analyses of Ralt esters revealed that they are extensively metabolized to mono or diacids and further

to demethylated forms and unidentified species. The cell pumps out the remaining diacid forms; the marginal fraction that remains unmodified and intracellular affords weak whole-cell activity. In sum, the lack of on-target whole-cell activity of Ralt-1 and its analogs with a 2-methyl-4-oxo quinazoline ring can be attributed to a combination of their poor uptake, efflux, and rapid metabolism, chiefly the last.

In sum, our quest for a PptT inhibitor by target-based HTS resulted in the most potent PptT inhibitor identified to date. An extensive SAR campaign was aided by access to a legacy collection of raltitrexed analogs at AstraZeneca together with targeted synthesis of additional analogs. This led to greater inhibitory potency, but not to potent whole-cell activity. Solution of the structure of a Ralt-1–PptT cocrystal and analysis of the intrabacterial fate of Ralt-1 and its analogs demonstrated that the shape of the enzyme's active site differs markedly depending on what binds to it; the inhibitors' targets vary markedly depending on minor substitutions; and *Mtb* protects itself by rapidly taking these molecules apart. We hope these lessons will be instructive for other anti-infective discovery campaigns.

MATERIALS AND METHODS

Purification of PptT

Recombinant PptT was purified from *Escherichia coli* as described (7, 20). Briefly, *E. coli* BL21 DE3 cells expressing pMCSG28-PptT were grown to an optical density at 600 nm (OD_{600}) of 0.6 to 0.8 in LB medium containing ampicillin (100 μ g/ml). Cultures were cold shocked on ice for 20 min and then induced overnight at 16°C with 1 mM isopropyl- β -D-thiogalactopyranoside (IPTG). Induced cells were pelleted at 5000g and resuspended in lysis buffer [50 mM MES (pH 6.7), 250 mM NaCl, 50 mM L-Glu, 50 mM L-Arg, 10 mM $MgCl_2$, 5 mM imidazole, 1 mM dithiothreitol (DTT), and 10% glycerol] supplemented with deoxyribonuclease (DNase; 20 μ g/ml) and lysozyme (0.2 mg/ml). The resuspended cells were lysed using a Emulsiflex C5 high pressure homogenizer, followed by centrifugation at 14,000g for 45 min at 4°C. The resulting supernatant was incubated with a pre-equilibrated Ni-nitrilotriacetic acid (Ni-NTA) resin with gentle rocking at 4°C. Beads were loaded onto a gravity column and washed with lysis buffer. The bound PptT protein was eluted with elution buffer [50 mM MES (pH 6.7), 250 mM NaCl, 50 mM L-Glu, 50 mM L-Arg, 10 mM $MgCl_2$, 1 mM DTT, 300 mM imidazole, and 10% glycerol]. The eluted fractions were pooled and loaded onto an HiLoad Superdex 75 pg gel filtration column pre-equilibrated with gel filtration buffer [50 mM MES (pH 5.8), 250 mM NaCl, 50 mM L-Glu, 50 mM L-Arg, 10 mM $MgCl_2$, 1 mM DTT, and 10% glycerol] and fractionated with an AKTA pure fast protein liquid chromatography system (fig. S1A). The purity of the eluted fractions corresponding to monomer of PptT was verified by 12.5% SDS–polyacrylamide gel electrophoresis (SDS-PAGE; fig. S1A). PptT-containing fractions were pooled and concentrated to 4 mg/ml using 10-kDa molecular weight cut-off Centricon centrifugal filter units. The glycerol concentration was adjusted to 50%. The aliquots were flash-frozen with liquid N_2 and stored at -80°C .

Purification of N-ACP PKS13

The N-terminal ACP module (N-ACP) of PKS13 was cloned in the pMCSG7 plasmid to obtain expression of the N-domain ACP of PKS13 with a 6XHis tag and an additional stretch of amino acids (SSGVDLGTENLYFQSNA) at the N terminus. For expression and

purification, the *E. coli* BL21 Δ entD strain was transformed with the pMCSG7-PKS13 construct and selected on LB plates containing ampicillin at 100 μ g/ml. Cells were grown to an OD_{600} 0.8 to 0.9 and cold shocked on ice for 20 min. Protein expression was then induced with 1 mM IPTG for 4 hours at 30°C. Cells were harvested by centrifugation (6000 rpm for 15 min at 4°C) and resuspended in lysis buffer [50 mM tris (pH 7.8), 200 mM NaCl, 5 mM imidazole, and 10% glycerol] supplemented with DNase (20 μ g/ml) and lysozyme (0.2 mg/ml). Induced cells were harvested by centrifugation and lysed using an Emulsiflex C5 high pressure homogenizer. The resulting lysates were centrifuged at 14000 rpm for 45 min. The supernatant was collected and mixed with pre-equilibrated Ni-NTA beads and gently agitated on a rocker for 2 hours at 4°C. The beads were then loaded onto a gravity column and washed with 50 ml of lysis buffer followed by 50 ml of wash buffer [50 mM tris (pH 7.8), 20 mM NaCl, 10% glycerol, and 20 mM imidazole]. The bound protein was eluted with elution buffer [50 mM tris (pH 7.8), 20 mM NaCl, 10% glycerol, and 300 mM imidazole]. The eluted fractions were pooled, and proteins were further resolved on a HiTrap Q HP anion exchange column. Apo and holo N-ACP PKS13 were separated with a linear gradient of 20 to 500 mM NaCl in 50 mM tris (pH 7.8), 20 mM NaCl, and 10% glycerol. The first peak fractions corresponding to apo ACP were collected, concentrated to 5 mg/ml, aliquoted, flash-frozen in liquid N_2 , and stored at -80°C until use. Figure S1B illustrates the chromatogram and SDS-PAGE gel image of purified N-ACP PKS13.

FP-based PptT enzyme assay

Initial FP reactions were performed in 50 μ l of reaction volumes in 96-well black plates (Greiner, #M9685) in 100 mM MES (pH 6.5), 200 mM NaCl, 20 mM $MgCl_2$, 0.01% Tween 20, 25 μ M His-N-ACP PKS13 substrate, 2.5 μ M CoA-probe, and 200 nM PptT enzyme. The reaction was initiated by the addition of a mix of probe/enzyme. For CRC analysis, 2 μ l of test compounds (10 concentration points using a twofold dilution series from 100 to 0 μ M final concentration) was added to reaction wells, accounting for 4% of resulting dimethyl sulfoxide (DMSO). Reactions were incubated at room temperature, and plates were continuously monitored at 485/20 nm excitation and 485/20 nm emission for both parallel and perpendicular intensities using a BioTek Synergy NEO plate reader. For reactions in 384-well plates, reactions were set up in a 20- μ l reaction volume. To optimize the assay, reactions were performed in triplicates with varying PptT (20 to 500 nM), N-ACP PKS13 substrate (0 to 200 μ M), CoA-PEG-ACM-FL-BDP probe (0 to 25 μ M), DMSO (0 to 10%), reaction pH (6.5 to 8.5), and reducing agents [DTT and tris(2-carboxyethyl)phosphine (TCEP)]. After a 30-min incubation at room temperature (otherwise stated if for kinetic reads), the reactions were quenched by the addition of 50 mM EDTA, and then the FP signal was determined. The products formed were also resolved by 15% SDS-PAGE and visualized using a RGB scan for fluorescence signal (BDP-FL 488/503 nm). The total amount of the protein was quantified by Coomassie G-250 staining followed by densitometry using ImageJ.

High-throughput screening

Screening was conducted at the High Throughput Screening Resource Center at Rockefeller University. Pilot screening was initially performed using the LOPAC¹²⁸⁰. The repurposing collection of 6143 unique compounds contains legally approved drugs, investigational drugs that have been tested in clinical trials and pre-clinical compounds described in peer-reviewed or published

research. Screening reactions were carried out in a 20- μ l reaction volume in fluorimmunoassay compatible black 384-well plates (Greiner, #781076). Reaction components were dispensed in the plates in four steps to achieve a final concentration of 100 mM MES (pH 7), 200 mM NaCl, 20 mM MgCl₂, 8% DMSO, 25 μ M His-N-ACP PKS13 substrate, 2.5 μ M CoA-probe, 100 nM PptT enzyme, and 10 μ M test compounds using the following order: (i) Ten microliters of buffer A [100 mM MES (pH 7), 200 mM NaCl, and 20 mM MgCl₂] with 4.8% DMSO was added to each well using a Thermo Multidrop Combi dispenser (Thermo Fisher Scientific); (ii) 0.04 μ l of library compounds at 5 mM to columns 1 to 22 of the plates using a 384-well head pin tool (V&P Scientific) with a MDT Janus robot (PerkinElmer); (iii) 5 μ l of 100 μ M His-N-ACP PKS13 substrate and 1% DMSO in a mix with buffer A; and (iv) 5 μ l of 100 nM PptT/2.5 μ M BDP-CoA mix prepared in buffer A with 2% DMSO were added to columns 1 to 23; column 24 was filled with 5 μ l of this mix containing 10 μ M amidinourea 8918 as a positive control. After each step of adding reagents, plates were centrifuged at 1000 rpm for 30 s to collect all the liquid at the bottom of each well. The plates were then incubated at 30°C for 30 min for the enzymatic reaction. After incubation, reagents from well B24 were replaced with BDP-CoA-probe buffer mix (readouts were scaled to this well). The reactions were stopped with 50 mM EDTA. Fluorescence was recorded at 485/20 nm excitation λ and 485/20 nm emission λ for both parallel (I_{\parallel}) and perpendicular (I_{\perp}) relative fluorescence intensities using a BioTek Synergy NEO plate reader. To confirm hits, compounds were cherry-picked and retested in triplicates from screening stocks at 10 μ M in triplicate. For further validation, the confirmed hits were retested in dose-response (0 to 62.5 μ M). The purity of confirmed hits was checked using high-performance liquid chromatography. Chemical structures and assay results were archived and analyzed at Collaborative Drug Discovery (CDD) (Burlingame, CA www.collaborativedrug.com). Spotfire was used to help visualize data and to apply cutoff filters to identify compounds with drug-like properties and a lack of structural alerts.

Quantitation of screening data

As a measure for assay quality control, Z' scores were calculated using the formula $Z' = 1 - 3(\sigma^+ + \sigma^-)/|\mu^+ - \mu^-|$ as described (43), where σ^+ and σ^- represent SDs from the mean of positive signals and of negative signals, respectively, and μ^+ and μ^- represent the mean of positive signals and negative signals, respectively. The FP signal generated in each well with test compound (10 μ M) was normalized against the positive control in column 24 (reaction with 10 μ M 8918), and the negative control in column 23 (reaction without any test agent/inhibitor) as normalized percent of inhibition (NPI) = $[(FP_{\text{sample}} - FP_{\text{average negative control}})/(FP_{\text{average positive control}} - FP_{\text{average negative control}})] \times 100$.

IC₅₀ determinations

Compound stocks prepared in DMSO were dispensed in duplicate in 384-well black plates with an HP D300e Digital Dispenser to form two overlapping series spanning 10 concentrations resulting from twofold serial dilutions over the ranges 100 to 0.198 μ M and 10 to 0.0198 μ M. For potent inhibitors, the procedure was repeated to give final concentrations in the ranges 25 μ M to 48 nM and 2.5 μ M to 4.8 nM. The reaction conditions were 100 mM MES (pH 7), 200 mM NaCl, 20 mM MgCl₂, 8% DMSO, 0.005% Tween 20, 50 μ M His-N-ACP PKS13 substrate, 2.5 μ M CoA-probe, and 100 nM PptT enzyme.

FP data were normalized relative to the positive controls (wells with only probe) and negative controls (reaction well with DMSO) to evaluate % inhibition at each concentration. XY plots of concentration versus % inhibition were analyzed by variable slope (four parameter) nonlinear regression curve fit to determine IC₅₀ values.

Crystallization, data collection, and structure solution

PptT was produced and purified as described in (7) and in the Supplementary Materials, followed by cleavage of the His-tag by tobacco etch virus (TEV) protease and passage of the digestion mixture through Ni-NTA resin, which retained the His-tagged TEV, the digested tag peptide, and the residual undigested protein. Cleaved PptT was concentrated to 10 mg/ml and mixed with Ralt-1 at final concentration of 2 mM before setting into hanging vapor diffusion drops, mixing it in a 1:1 volume ratio with mother liquor [0.1 M tris-HCl (pH 8.0), 0.2 M NaCl, and 1 M Na/K tartrate]. Crystals were flash-frozen in 15% sucrose and 25% PEG 4000 in 0.1 M sodium phosphate at pH 7.2 before data collection. Data were collected at the Brookhaven National Lab NSLS synchrotron FMX beamline and indexed, integrated, and scaled by the beamline auto-processing pipeline [XDS (44), POINTLESS (45), and AIMLESS (46)] software packages. Anisotropic analysis of merged data, final correction, and estimation of structure amplitudes were done by STARANISO (Global Phasing Limited). The structure was solved by molecular replacement with Molrep software (47) using the 6CT5 PDB entry as a search model. This was followed by iterative cycles of refinement with PHENIX. REFINER and manual building in COOT (48, 49). A ligand model and restraints were created using the eLBOW tool (50).

Minimal inhibitory concentration determination

The activity of test compounds against *Mtb* H37Rv WT, *Mtb* mutant *pptT* cKD; DAS-PptT TetON-10, and *Mtb* *pptH* KO was determined as published (7, 20). *Mtb* strains were passaged in Middlebrook 7H9 medium containing 0.2% glycerol, 10% ADN [5% (w/v) albumin, 2% (w/v) dextrose, 0.85% (w/v) NaCl] supplement, and 0.02% tyloxapol at 37°C with 20% O₂ and 5% CO₂. The *pptH* KO strain was grown in the presence of hygromycin (50 μ g/ml), and the *pptT* cKD strain was grown in the presence of hygromycin (50 μ g/ml) and streptomycin (20 μ g/ml). The *pptT* cKD strain was grown with anhydrotetracycline (500 ng/ml; ATc) for 6 days, and to deplete PptT, cells were passaged in ATc-free medium for 6 days. Fifty microliters *Mtb* cells were dispensed in 384-well plates (Greiner, #781091) predisposed with compounds at an OD₅₈₀ of 0.01. The bacilli were exposed to the test compounds for 6 to 7 days (WT and *pptH* KO) or 9 to 10 days (*pptT* cKD +/− ATc), and the OD₅₈₀ was determined using a SpectraMax M5 (Molecular Devices) spectrophotometer. Inhibition (%) of growth was calculated by normalizing the OD₅₈₀'s of the sample well relative to the negative control (DMSO) and the positive control (100 μ M 8918). MICs were calculated by CDD using a Levenberg-Marquardt algorithm to fit a Hill equation to the dose-response data. Each test compound was tested in duplicate in at least in two independent experiments.

Intrabacterial pharmacokinetics: Sample preparation

Samples were prepared for metabolomics analyses according to a published protocol (40). Briefly, *Mtb* H37Rv was grown to mid-log phase (OD₅₈₀ of 0.6–0.7) in 7H9-ADN medium with 0.2% glycerol and 0.02% tyloxapol. Cells were washed with tyloxapol-free medium, inoculated at a density of 5×10^8 colony-forming units/ml onto 25-mm, 0.22- μ m polyvinylidene difluoride filters (Millipore) using

vacuum filtration, transferred onto 7H10-ADN agar plates, and incubated at 37°C for 5 days to allow bacterial growth. The filters were then transferred onto swimming pool caps containing Sauton's medium and 10 μ M of Ralt-1, **2t**, **2r**, **2s**, or **2d**. After 24 hours of compound exposure, cell metabolism was quenched by freezing *Mtb*-laden filters in ice-cold acetonitrile:methanol:H₂O (40:40:20). Cells were lysed using a temperature-controlled beat beater/homogenizer (Precellys) with cooling on ice between steps. The extracts were purified by centrifugation and filtration through 0.22- μ m nylon spin-X columns (Costar, #CLS6189). The extracellular medium was collected for analysis, including from control samples without bacteria. Each experiment was performed once with three technical replicates for each compound.

LC-MS analysis

Aliquots from each sample of medium (100 μ l) were added to 400 μ l of 1:1 acetonitrile/methanol, mixed with 500 μ l of acetonitrile + 0.2% formic acid, and then centrifuged at 13,000g for 10 min at 4°C to pellet precipitates. Lysates were combined 1:1 with acetonitrile + 0.2% formic acid and processed similarly. Supernatants were transferred into mass spectrometry vials and analyzed using a semiquantitative LC/MS-based method as described (38). Samples were separated on a Cogent Diamond Hydride Type C column (Microsolv Technologies) using a 2- μ l injection volume on an Agilent 1200 Series LC system coupled to an Agilent 6546 quadrupole time of flight mass spectrometer in positive acquisition mode. The mobile phase consisted of solvent A (double-distilled H₂O with 0.2% formic acid) and solvent B (acetonitrile with 0.2% formic acid), and the gradient used was as follows: 0 to 2 min, 85% B; 3 to 5 min, 80% B; 6 to 7 min, 75% B; 8 to 9 min, 70% B; 10 to 11.1 min, 50% B; 11.1 to 14 min 20% B; 14.1 to 24 min 5% B, followed by a 10-min re-equilibration period of 85% B at a flow rate of 0.4 ml/min. Dynamic mass axis calibration was achieved by continuous infusion of a reference mass solution using an isocratic pump with a 100:1 splitter. Data were analyzed using Agilent MassHunter Qualitative Analysis Navigator software to measure relative levels of the [M + H]⁺ ion (\pm 100 ppm). To determine uptake, test compound levels in bacteria-laden filter swimming pools were compared to levels from control swimming pools incubated with cell-free filters under the same conditions, and metabolism was determined by comparing test compound levels from cell lysates and media. Putative biotransformation products were identified in cell lysates after treatment with 100 μ M **2d**, using pairwise comparisons on XCMS online (51). For LC-MS/MS, the same separation gradient was used. Collision was performed at 10 eV using a parent ion mass of either 445 or 459 with a narrow (1.3 amu) isolation width.

Other methods

Methods are presented in the online Supplementary Materials for generation of *E. coli* BL21 Δ entD strain, differential scanning fluorimetry, Vina docking, DHFR activity assay, preincubation and rapid dilution assay, isothermal titration calorimetry, and general procedure for coupling of CoA with fluorescent probes.

Supplementary Materials

This PDF file includes:

Supplementary Materials Text
Supplementary Methods
Figs. S1 to S9
Tables S1 to S7

REFERENCES AND NOTES

1. C. Nathan, Fresh approaches to anti-infective therapies. *Sci. Transl. Med.* **4**, 140sr142 (2012).
2. S. M. Schrader, J. Vaubourgeix, C. Nathan, Biology of antimicrobial resistance and approaches to combat it. *Sci. Transl. Med.* **12**, (2020).
3. M. A. Cook, G. D. Wright, The past, present, and future of antibiotics. *Sci. Transl. Med.* **14**, eabo7793 (2022).
4. B. Gold, J. Zhang, L. L. Quezada, J. Roberts, Y. Ling, M. Wood, W. Shinwari, L. Goullieux, C. Roubert, L. Fraisse, E. Bacqué, S. Lagrange, B. Flöche-Rommé, M. Vieth, P. A. Hipskind, L. N. Jungheim, J. Aubé, S. M. Scarry, S. L. McDonald, K. Li, A. Perkowski, Q. Nguyen, V. Dartois, M. Zimmerman, D. B. Olsen, K. Young, S. Bonnett, D. Joerss, T. Parish, H. I. Boshoff, K. Arora, C. E. Barry III, L. Guíjarro, S. Anca, J. Rullas, B. Rodríguez-Salguero, M. S. Martínez-Martínez, E. Porras-de Francisco, M. Cacho, D. Barros-Aguirre, P. Smith, S. J. Berthel, C. Nathan, R. H. Bates, Identification of β -Lactams active against *Mycobacterium tuberculosis* by a consortium of pharmaceutical companies and academic institutions. *ACS Infect. Dis.* **8**, 557–573 (2022).
5. B. B. Aldridge, D. Barros-Aguirre, C. E. Barry III, R. H. Bates, S. J. Berthel, H. I. Boshoff, K. Chibale, X. J. Chu, C. B. Cooper, V. Dartois, K. Duncan, N. Fotouhi, F. Gusovsky, P. A. Hipskind, D. J. Kempf, J. Lelièvre, A. J. Lenaerts, C. W. McNamara, V. Mizrahi, C. Nathan, D. B. Olsen, T. Parish, H. M. Petrassi, A. Pym, K. Y. Rhee, G. T. Robertson, J. M. Rock, E. J. Rubin, B. Russell, D. G. Russell, J. C. Sacchettini, D. Schnappinger, M. Schrimpf, A. M. Upton, P. Warner, P. G. Wyatt, Y. Yuan, The tuberculosis drug accelerator at year 10: What have we learned? *Nat. Med.* **27**, 1333–1337 (2021).
6. D. J. Payne, M. N. Gwynn, D. J. Holmes, D. L. Pompliano, Drugs for bad bugs: Confronting the challenges of antibacterial discovery. *Nat. Rev. Drug Discov.* **6**, 29–40 (2007).
7. E. Ballinger, J. Mosior, T. Hartman, K. Burns-Huang, B. Gold, R. Morris, L. Goullieux, I. Blanc, J. Vaubourgeix, S. Lagrange, L. Fraisse, S. Sans, C. Couturier, E. Bacqué, K. Rhee, S. M. Scarry, J. Aubé, G. Yang, O. Ouerfelli, D. Schnappinger, T. R. Ioerger, C. A. Engelhart, J. A. McConnell, K. McAulay, A. Fay, C. Roubert, J. Sacchettini, C. Nathan, Opposing reactions in coenzyme A metabolism sensitize *Mycobacterium tuberculosis* to enzyme inhibition. *Science* **363**, (2019).
8. C. Chalut, L. Botella, C. de Sousa-D'Auria, C. Houssin, C. Guilhot, The nonredundant roles of two 4'-phosphopantetheinyl transferases in vital processes of *Mycobacteria*. *Proc. Natl. Acad. Sci. U.S.A.* **103**, 8511–8516 (2006).
9. C. Leblanc, T. Prudhomme, G. Tabouret, A. Ray, S. Burbaud, S. Cabantous, L. Mourey, C. Guilhot, C. Chalut, 4'-Phosphopantetheinyl transferase PptT, a new drug target required for *Mycobacterium tuberculosis* growth and persistence in vivo. *PLOS Pathog.* **8**, e1003097 (2012).
10. C. R. Vickery, N. M. Kosa, E. P. Casavant, S. Duan, J. P. Noel, M. D. Burkart, Structure, biochemistry, and inhibition of essential 4'-phosphopantetheinyl transferases from two species of *Mycobacteria*. *ACS Chem. Biol.* **9**, 1939–1944 (2014).
11. O. Zimhony, A. Schwarz, M. Raitses-Gurevich, Y. Peleg, O. Dym, S. Albeck, Y. Burstein, Z. Shakked, AcpM, the meromycolate extension acyl carrier protein of *Mycobacterium tuberculosis*, is activated by the 4'-phosphopantetheinyl transferase PptT, a potential target of the multistep mycolic acid biosynthesis. *Biochemistry* **54**, 2360–2371 (2015).
12. J. Beld, E. C. Sonnenschein, C. R. Vickery, J. P. Noel, M. D. Burkart, The phosphopantetheinyl transferases: Catalysis of a post-translational modification crucial for life. *Nat. Prod. Rep.* **31**, 61–108 (2014).
13. P. J. Brennan, Structure, function, and biogenesis of the cell wall of *Mycobacterium tuberculosis*. *Tuberculosis (Edinb.)* **83**, 91–97 (2003).
14. A. M. Block, S. B. Namugenyi, N. P. Palani, A. M. Brokaw, L. Zhang, K. B. Beckman, A. D. Tischler, *Mycobacterium tuberculosis* requires the outer membrane lipid phthiocerol dimycocerosate for starvation-induced antibiotic tolerance. *mSystems* **8**, e0069922 (2023).
15. C. R. Ruhl, B. L. Pasko, H. S. Khan, L. M. Kindt, C. E. Stamm, L. H. Franco, C. C. Hsia, M. Zhou, C. R. Davis, T. Qin, L. Gautron, M. D. Burton, G. L. Mejia, D. K. Naik, G. Dussor, T. J. Price, M. U. Shiloh, *Mycobacterium tuberculosis* Sulfolipid-1 activates nociceptive neurons and induces cough. *Cell* **181**, 293–305.e11 (2020).
16. C. Carivenc, L. Maveyraud, C. Blanger, S. Ballereau, C. Roy-Camille, M. C. Nguyen, Y. Génisson, C. Guilhot, C. Chalut, J. D. Pedelacq, L. Mourey, Phosphopantetheinyl transferase binding and inhibition by amidino-urea and hydroxypyrimidinethione compounds. *Sci. Rep.* **11**, 18042 (2021).
17. A. Rohilla, G. Khare, A. K. Tyagi, A combination of docking and cheminformatics approaches for the identification of inhibitors against 4' phosphopantetheinyl transferase of *Mycobacterium tuberculosis*. *RSC Adv.* **8**, 328–341 (2018).
18. J. Mosior, R. Bourland, S. Soma, C. Nathan, J. Sacchettini, Structural insights into phosphopantetheinyl hydrolase PptH from *Mycobacterium tuberculosis*. *Protein Sci.* **29**, 744–757 (2020).
19. S. Pandey, A. Singh, G. Yang, F. B. d'Andrea, X. Jiang, T. E. Hartman, J. W. Mosior, R. Bourland, B. Gold, J. Roberts, A. Geiger, S. Tang, K. Rhee, O. Ouerfelli, J. C. Sacchettini, C. F. Nathan, K. Burns-Huang, Characterization of phosphopantetheinyl hydrolase from *Mycobacterium tuberculosis*. *Microbiol Spectr* **9**, e0092821 (2021).

20. S. Ottavi, S. M. Scarry, J. Mosior, Y. Ling, J. Roberts, A. Singh, D. Zhang, L. Goullieux, C. Roubert, E. Bacqué, H. R. Lagiokas, J. Vendome, F. Moraca, K. Li, A. J. Perkowski, R. Ramesh, M. M. Bowler, W. Tracy, V. A. Feher, J. C. Sacchettini, B. S. Gold, C. F. Nathan, J. Aubé, *In vitro* and *in vivo* inhibition of the *Mycobacterium tuberculosis* phosphopantetheinyl transferase PptT by amidinouras. *J. Med. Chem.* **65**, 1996–2022 (2022).
21. S. Ottavi, K. Li, J. G. Cacioppo, A. J. Perkowski, R. Ramesh, B. S. Gold, Y. Ling, J. Roberts, A. Singh, D. Zhang, J. Mosior, L. Goullieux, C. Roubert, E. Bacqué, J. C. Sacchettini, C. F. Nathan, J. Aubé, *Mycobacterium tuberculosis* PptT inhibitors based on heterocyclic replacements of amidinouras. *ACS Med. Chem. Lett.* **14**, 970–976 (2023).
22. A. S. Brown, J. G. Owen, J. Jung, E. N. Baker, D. F. Ackerley, Inhibition of indigoidine synthesis as a high-throughput colourimetric screen for antibiotics targeting the essential *Mycobacterium tuberculosis* phosphopantetheinyl transferase PptT. *Pharmaceutics* **13**, (2021).
23. J. G. Owen, J. N. Copp, D. F. Ackerley, Rapid and flexible biochemical assays for evaluating 4'-phosphopantetheinyl transferase activity. *Biochem. J.* **436**, 709–717 (2011).
24. B. P. Duckworth, C. C. Aldrich, Development of a high-throughput fluorescence polarization assay for the discovery of phosphopantetheinyl transferase inhibitors. *Anal. Biochem.* **403**, 13–19 (2010).
25. E. M. Bowers, G. Yan, C. Mukherjee, A. Orry, L. Wang, M. A. Holbert, N. T. Crump, C. A. Hazzalin, G. Liszczak, H. Yuan, C. Larooca, S. A. Saldanha, R. Abagyan, Y. Sun, D. J. Meyers, R. Marmorstein, L. C. Mahadevan, R. M. Alani, P. A. Cole, Virtual ligand screening of the p300/CBP histone acetyltransferase: Identification of a selective small molecule inhibitor. *Chem. Biol.* **17**, 471–482 (2010).
26. A. McCluskey, J. A. Daniel, G. Hadzic, N. Chau, E. L. Clayton, A. Mariana, A. Whiting, N. N. Gorgani, J. Lloyd, A. Quan, L. Moshkanbaryans, S. Krishnan, S. Perera, M. Chircop, L. von Kleist, A. B. McGeachie, M. T. Howes, R. G. Parton, M. Campbell, J. A. Sakoff, X. Wang, J. Y. Sun, M. J. Robertson, F. M. Deane, T. H. Nguyen, F. A. Meunier, M. A. Cousin, P. J. Robinson, Building a better dynasore: The dyngo compounds potently inhibit dynamin and endocytosis. *Traffic* **14**, 1272–1289 (2013).
27. E. Van Cutsem, Raltitrexed (Tomudex). *Expert Opin. Investig. Drugs* **7**, 823–834 (1998).
28. S. A. Lawrence, S. A. Titus, J. Ferguson, A. L. Heineman, S. M. Taylor, R. G. Moran, Mammalian mitochondrial and cytosolic folypolyglutamate synthetase maintain the subcellular compartmentalization of folates. *J. Biol. Chem.* **289**, 29386–29396 (2014).
29. E. M. Berman, L. M. Werbel, D. J. McNamara, Substituted quinazolinones as anticancer agents. *Google Patents US4857530A*, (1989).
30. D. Pires, E. Valente, M. F. Simões, N. Carmo, B. Testa, L. Constantino, E. Anes, Esters of pyrazinoic acid are active against pyrazinamide-resistant strains of *Mycobacterium tuberculosis* and other naturally resistant *Mycobacteria in vitro* and *ex vivo* within macrophages. *Antimicrob. Agents Chemother.* **59**, 7693–7699 (2015).
31. E. Van Cutsem, D. Cunningham, J. Maroun, A. Cervantes, B. Glimelius, Raltitrexed: Current clinical status and future directions. *Ann. Oncol.* **13**, 513–522 (2002).
32. D. Gramec, L. Peterlin Mašič, M. Sollner Dolenc, Bioactivation potential of thiophene-containing drugs. *Chem. Res. Toxicol.* **27**, 1344–1358 (2014).
33. E. M. Larsen, R. J. Johnson, Microbial esterases and ester prodrugs: An unlikely marriage for combating antibiotic resistance. *Drug Dev. Res.* **80**, 33–47 (2019).
34. P. Lassalas, B. Gay, C. Lasfargeas, M. J. James, V. Tran, K. G. Vijayendran, K. R. Brunden, M. C. Kozlowski, C. J. Thomas, A. B. Smith III, D. M. Hurny, C. Ballatore, Structure property relationships of carboxylic acid isosteres. *J. Med. Chem.* **59**, 3183–3203 (2016).
35. B. Hajian, E. Scocchera, C. Shoen, J. Krucinska, K. Viswanathan, N. G-Dayanandan, H. Erlandsen, A. Estrada, K. Mikušová, J. Korduláková, M. Cynamon, D. Wright, Drugging the Folate Pathway in *Mycobacterium tuberculosis*: The role of multi-targeting Agents. *Chem. Biol.* **26**, 781–791.e6 (2019).
36. J. P. Santa Maria Jr., Y. Park, L. Yang, N. Murgolo, M. D. Altman, P. Zuck, G. Adam, C. Chamberlin, P. Saradjian, P. Dandliker, H. I. M. Boshoff, C. E. B. Rd, C. Garlisi, D. B. Olsen, K. Young, M. Glick, E. Nickbarg, P. S. Kutchukian, Linking high-throughput screens to identify MoAs and novel inhibitors of *Mycobacterium tuberculosis* dihydrofolate reductase. *ACS Chem. Biol.* **12**, 2448–2456 (2017).
37. Q. Wan, B. C. Bennett, T. Wymore, Z. Li, M. A. Wilson, C. L. Brooks III, P. Langan, A. Kovalevsky, C. G. Dealwis, Capturing the catalytic proton of dihydrofolate reductase: Implications for general acid-base catalysis. *ACS Catal.* **11**, 5873–5884 (2021).
38. I. D. Kuntz, K. Chen, K. A. Sharp, P. A. Kollman, The maximal affinity of ligands. *Proc. Natl. Acad. Sci. U.S.A.* **96**, 9997–10002 (1999).
39. A. L. Hopkins, C. R. Groom, A. Alex, Ligand efficiency: A useful metric for lead selection. *Drug Discov. Today* **9**, 430–431 (2004).
40. K. A. Planck, K. Rhee, Metabolomics of *Mycobacterium tuberculosis*. *Methods Mol. Biol.* **2314**, 579–593 (2021).
41. B. Bosch, M. A. DeJesus, N. C. Poulton, W. Zhang, C. A. Engelhart, A. Zaveri, S. Lavalette, N. Ruecker, C. Trujillo, J. B. Wallach, S. Li, S. Ehr, B. T. Chait, D. Schnappinger, J. M. Rock, Genome-wide gene expression tuning reveals diverse vulnerabilities of *M. tuberculosis*. *Cell* **184**, 4579–4592.e24 (2021).
42. M. R. Nixon, K. W. Saionz, M. S. Koo, M. J. Szymonifka, H. Jung, J. P. Roberts, M. Nandakumar, A. Kumar, R. Liao, T. Rustad, J. C. Sacchettini, K. Y. Rhee, J. S. Freundlich, D. R. Sherman, Folate pathway disruption leads to critical disruption of methionine derivatives in *Mycobacterium tuberculosis*. *Chem. Biol.* **21**, 819–830 (2014).
43. J. H. Zhang, T. D. Chung, K. R. Oldenburg, A Simple statistical parameter for use in evaluation and validation of high throughput screening assays. *J. Biomol. Screen.* **4**, 67–73 (1999).
44. W. Kabsch, XDS. *Acta Crystallogr. D Biol. Crystallogr.* **66**, 125–132 (2010).
45. P. Evans, Scaling and assessment of data quality. *Acta Crystallogr. D Biol. Crystallogr.* **62**, 72–82 (2006).
46. P. R. Evans, G. N. Murshudov, How good are my data and what is the resolution? *Acta Crystallogr. D Biol. Crystallogr.* **69**, 1204–1214 (2013).
47. A. Vagin, A. Teplyakov, Molecular replacement with MOLREP. *Acta Crystallogr. D Biol. Crystallogr.* **66**, 22–25 (2010).
48. P. Emsley, K. Cowtan, Coot: Model-building tools for molecular graphics. *Acta Crystallogr. D Biol. Crystallogr.* **60**, 2126–2132 (2004).
49. D. Liebschner, P. V. Afonine, M. L. Baker, G. Bunkóczi, V. B. Chen, T. I. Croll, B. Hintze, L. W. Hung, S. Jain, A. J. McCoy, N. W. Moriarty, R. D. Oeffner, B. K. Poon, M. G. Prisant, R. J. Read, J. S. Richardson, D. C. Richardson, M. D. Sammito, O. V. Sobolev, D. H. Stockwell, T. C. Terwilliger, A. G. Urzhumtsev, L. L. Videau, C. J. Williams, P. D. Adams, Macromolecular structure determination using X-rays, neutrons and electrons: Recent developments in Phenix. *Acta Crystallogr. D Struct. Biol.* **75**, 861–877 (2019).
50. N. W. Moriarty, R. W. Grosse-Kunstleve, P. D., Electronic ligand builder and optimization workbench (eLBOW): A tool for ligand coordinate and restraint generation. *Acta Crystallogr. D Biol. Crystallogr.* **65**, 1074–1080 (2009).
51. C. A. Smith, E. J. Want, G. O'Maille, R. Abagyan, G. Siuzdak, XCMS: Processing mass spectrometry data for metabolite profiling using nonlinear peak alignment, matching, and identification. *Anal. Chem.* **78**, 779–787 (2006).
52. K. C. Murphy, K. G. Campellone, Lambda Red-mediated recombinogenic engineering of enterohemorrhagic and enteropathogenic *E. coli*. *BMC Mol. Biol.* **4**, 11 (2003).
53. F. H. Niesen, H. Berglund, M. Vedadi, The use of differential scanning fluorimetry to detect ligand interactions that promote protein stability. *Nat. Protoc.* **2**, 2212–2221 (2007).
54. O. Trott, A. J. Olson, AutoDock Vina: Improving the speed and accuracy of docking with a new scoring function, efficient optimization, and multithreading. *J. Comput. Chem.* **31**, 455–461 (2010).
55. J. Eberhardt, D. Santos-Martins, A. F. Tillack, S. Forli, AutoDock Vina 1.2.0: New docking methods, expanded force field, and python bindings. *J. Chem. Inf. Model.* **61**, 3891–3898 (2021).
56. A. Brecht, F. Beaufils. (2009), Drug transfer based on Coenzyme A and Acyl carrier protein. *US20110014216* (2009).
57. P. Bottari, R. Aebersold, F. Turecek, M. H. Gelb, Design and synthesis of visible isotope-coded affinity tags for the absolute quantification of specific proteins in complex mixtures. *Bioconjug. Chem.* **15**, 380–388 (2004).
58. T. Warriar, K. Kapilashrami, A. Argyrou, T. R. Ioerger, D. Little, K. C. Murphy, M. Nandakumar, S. Park, B. Gold, J. Mi, T. Zhang, E. Meiler, M. Rees, S. Somersan-Karakaya, E. Porras-de Francisco, M. Martinez-Hoyos, K. Burns-Huang, J. Roberts, Y. Ling, K. Y. Rhee, A. Mendoza-Losana, M. Luo, C. F. Nathan, N-methylation of a bactericidal compound as a resistance mechanism in *Mycobacterium tuberculosis*. *Proc. Natl. Acad. Sci. U.S.A.* **113**, E4523–E4530 (2016).
59. L. Zhao et al., Preparation of imidazopyrazines as protein kinase inhibitors. *Schering Corporation* (2007).
60. Z. Chen, F. Chen, Synthesis of pyrimidine compounds substituted by five membered heterocycles. *Jilin Huagong Xueyuan Xuebao* **30**, 47–50 (2013).
61. S. Ruan, L. Xu, M. Yu, N. Yu. Method for synthesizing Raltitrexed intermediate. *Shanghai DingYa Pharmaceutical Chemicals Co., Ltd.* (2018).
62. J. Inglese, G. Rai Bantukallu, S. Rana, L. Lamy. Preparation of methotrexate analogs and methotrexate-PROTAC analogs as DHFR degraders and their therapeutic uses. *United States Dept. 3of Health and Human Services* (2021).
63. S.-L. Cao, R. Wan, Y.-P. Feng, New synthesis of thymidylate synthase inhibitor Raltitrexed. *Synth. Commun.* **33**, 3519–3526 (2003).
64. J. Yang, X. Hu, Z. Liu, X. Li, Y. Dong, G. Liu, Cp*CollI-catalyzed formal [4+2] cycloaddition of benzamides to afford quinazolinone derivatives. *Chem. Commun.* **55**, 13840–13843 (2019).
65. X. Zhan, Y. Xu, Q. Qi, Y. Wang, H. Shi, Z. Mao, Synthesis, cytotoxic, and antibacterial evaluation of quinazolinone derivatives with substituted amino moiety. *Chem. Biodivers.* **15**, (2018).
66. Z. Zhao. Improved method for preparing Leitiqusai (raltitrexed). *Lunan Pharmaceutical Co., Ltd.* (2004).
67. S. Ruan, J. Zhan, G. Yan, L. Xu. Synthesis method of raltitrexed. *Shanghai DingYa Pharmaceutical Chemicals Co., Ltd.* (2015).
68. G. M. F. Bisset, K. Pawelczak, A. L. Jackman, A. H. Calvert, L. R. Hughes, Syntheses and thymidylate synthase inhibitory activity of the poly- γ -glutamyl conjugates of N-[5-[N-(3,4-dihydro-2-methyl-4-oxoquinazolin-6-ylmethyl)-N-methylamino]-2-thenoyl]-L-glutamic acid (ICI D1694) and other quinazolinone antifolates. *J. Med. Chem.* **35**, 859–866 (1992).

69. A. Presser, A. Hufner, Trimethylsilyldiazomethane—a mild and efficient reagent for the methylation of carboxylic acids and alcohols in natural products. *Monatsh. Chem.* **135**, 1015–1022 (2004).
70. H. Yuan, R. B. Silverman, New substrates and inhibitors of γ -aminobutyric acid aminotransferase containing bioisosteres of the carboxylic acid group: Design, synthesis, and biological activity. *Bioorg. Med. Chem.* **14**, 1331–1338 (2006).
71. C. Cardenal, S. B. L. Vollrath, U. Schepers, S. Brase, Synthesis of functionalized glutamine- and asparagine-type peptoids - scope and limitations. *Helv. Chim. Acta* **95**, 2237–2248 (2012).
72. H. Huang, P. Martasek, L. J. Roman, R. B. Silverman, Synthesis and evaluation of peptidomimetics as selective inhibitors and active site probes of nitric oxide synthases. *J. Med. Chem.* **43**, 2938–2945 (2000).
73. K.-y. Hung, P. W. R. Harris, M. A. Brimble, Use of 'click chemistry' for the synthesis of tetrazole-containing analogues of the neuroprotective agent glycyl-L-prolyl-L-glutamic acid. *Synlett* **2009**, 1233–1236 (2009).
74. V. B. Felber, M. A. Valentin, H.-J. Wester, Dual mode radiotracer and -therapeutics. *TUM*, (2022).
75. V. Bavetsias, J. H. Marriott, C. Melin, R. Kimbell, Z. S. Matusiak, F. T. Boyle, A. L. Jackman, Design and Synthesis of cyclopenta[*g*]quinazoline-based antifolates as inhibitors of thymidylate synthase and potential antitumor agents. *J. Med. Chem.* **43**, 1910–1926 (2000).
76. D. J. Antonjuk, D. K. Boadle, H. T. A. Cheung, T. Q. Tran, Synthesis of monoamides of methotrexate from L-glutamic acid monoamide tert-butyl esters. *J. Chem. Soc., Perkin Trans. 1*, 1989–2003 (1984).
77. S. Guo, M. Wu, M. Xu, H. Xu, L. Song, F. Li, Y. Liu. Preparation of benzodiazepine heterocyclic compounds. Zhejiang Jingxin Pharmaceutical Co., Ltd. Shanghai Jingxin Biology & Pharmaceutical Co. Ltd. (2020).
78. A. L. Smith, P. E. Brennan, F. F. Demorin, G. Liu, N. A. Paras, D. M. Retz. Aminopyrimidine compounds as polo-like kinase 1 inhibitors and their preparation, pharmaceutical compositions and use for treatment of cancer. *Amgen, Inc.* (2006).
79. S. Li, C. Yang, B. Yang, G. Li, Q. Gao, B. Zheng. (Shanghai Haoyuan Medchemexpress Co. Ltd., 2015).
80. J. J. Wade, Synthesis of imidazo[1,5-*c*]pyrimidine derivatives. *J. Heterocyclic Chem.* **23**, 981–987 (1986).
81. L. R. Hughes, J. Oldfield, S. J. Pegg, A. J. Barker, P. R. Marsham. Preparation of quinazolinone derivatives as anti-tumor agents. Imperial Chemical Industries PLC National Research Development Corp. (1990).
82. L. R. Hughes, A. L. Jackman, J. Oldfield, R. C. Smith, K. D. Burrows, P. R. Marsham, J. A. M. Bishop, T. R. Jones, B. M. O'Connor, A. H. Calvert, Quinazoline antifolate thymidylate synthase inhibitors: Alkyl, substituted alkyl, and aryl substituents in the C-2 position. *J. Med. Chem.* **33**, 3060–3067 (1990).
83. M. H. Block, C. S. Donald, K. M. Foote, D. R. Brittain. Preparation of amino substituted dibenzothiophenes for the treatment of disorders mediated by the neuropeptide Y5 receptor. AstraZeneca AB AstraZeneca UK Limited (2001).
84. J. D. Gass, A. Meister, 1-amino-1,3-dicarboxycyclohexane (cycloglutamic acid), a new glutamic acid analog and a substrate of glutamine synthetase. *Biochemistry* **9**, 842–846 (1970).
85. T. R. Jones, A. H. Calvert, A. L. Jackman, S. J. Brown, M. Jones, K. R. Harrap, A potent antitumour quinazoline inhibitor of thymidylate synthetase: Synthesis, biological properties and therapeutic results in mice. *Eur. J. Cancer* **17**, 11–19 (1981).
86. A. Hallberg, J. Westman, C. Post, Preparation of 2-aminoquinazoline derivatives and their therapeutic uses. *Softcure Pharmaceuticals AB*, (2008).
87. K. Pawelczak, T. R. Jones, M. Kempny, A. L. Jackman, D. R. Newell, L. Krzyzanowski, B. Rzeszotarska, Quinazoline antifolates inhibiting thymidylate synthase: Synthesis of four oligo(L- γ -glutamyl) conjugates of N10-propargyl-5,8-dideazafofolic acid and their enzyme inhibition. *J. Med. Chem.* **32**, 160–165 (1989).
88. J. R. Piper, N. D. Malik, M. S. Rhee, J. Galivan, F. M. Sirotnak, Synthesis and antifolate evaluation of the 10-propargyl derivatives of 5-deazafofolic acid, 5-deazaaminopterin, and 5-methyl-5-deazaaminopterin. *J. Med. Chem.* **35**, 332–337 (1992).
89. R. C. Elgersma, T. Huijbregts, D. C. J. Waalboer, J. A. F. Joosten, C. A. Beuckens-Schortinghuis, Antifolate linker-drugs and antibody-drug conjugates. *Byondis B.V.*, (2022).
90. J. B. Hynes, A. Kumar, A. Tomazic, W. L., Synthesis of 5-chloro-5,8-dideaza analogs of folic acid and aminopterin targeted for colon adenocarcinoma. *J. Med. Chem.* **30**, 1515–1519 (1987).
91. S. A. Patil, B. Shane, J. H. Freisheim, S. K. Singh, J. B. Hynes, Inhibition of mammalian folylpolyglutamate synthetase and human dihydrofolate reductase by 5,8-dideaza analogs of folic acid and aminopterin bearing a terminal L-ornithine. *J. Med. Chem.* **32**, 1559–1565 (1989).
92. J. Peiró Cadahia, J. Bondebjerg, C. A. Hansen, V. Previtali, A. E. Hansen, T. L. Andresen, Synthesis and evaluation of hydrogen peroxide sensitive prodrugs of methotrexate and aminopterin for the treatment of rheumatoid arthritis. *J. Med. Chem.* **61**, 3503–3515 (2018).

Acknowledgments: We acknowledge advice from P. Warner, Bill & Melinda Gates Foundation, Seattle, WA, USA and S. J. Berthel, Panorama Global, Seattle, WA, USA. We are grateful to D. Segura-Carro and R. H. Bates from GSK, Tres Cantos, Spain and E. Nickbarg and D. Olsen of Merck & Co. Inc., West Point, PA, USA for sharing raltitrexed analogs. We thank J. F. Glickman, M.-R. Menezes, and C. Larson from the High-Throughput and Spectroscopy Resource Center, Rockefeller University, New York, USA for HTS guidance and technical support. We thank D. Schnappinger, WCM, USA for help in recombineering and E. Clary, Texas A&M, USA for help in activity assay. We thank G. Sukenick and R. Wang of the NMR Analytical Core Facility, MSKCC for help in NMR and LC-MS analyses. **Funding:** This work was supported by grants OPP1190511 and INV-004709 to WCM, INV-002431 to Evotec, INV-040487 to Texas A&M and contract INV-020974 with AMG, all from the Bill & Melinda Gates Foundation; and P01AI095208 to Texas A&M, NIAID U19 AI162584 and F31AI154832 to WCM, and AI155510 to UNC from the National Institutes of Health, as well as by the Global Alliance for TB Drug Development and the Abby and Howard P. Milstein Program in Chemical Biology and Translational Medicine at WCM and the Welch Foundation grant A-0015 to Texas A&M. The Department of Microbiology & Immunology at WCM acknowledges the support of the William Randolph Hearst Foundation. The Organic Synthesis Core Facility at MSKCC acknowledges support by NCI Core Grants P30 CA008748 55 and NCI R50 CA243895 03. D.M.S., A.M.D., and M.P. are employees and shareholders of AstraZeneca UK Ltd. **Author contributions:** Designed research: C.N., A.S., J.A., and N.F. Conducted the screening and biochemical work: A.S. Contributed to compound design and synthesis: S.O., A.P., T.K., N.F., and J.A. Contributed to activity assay and performed the structural work: I.K., J.M., and J.C.S. Performed modeling studies: A.A. and M.G. Synthesized the probe: O.O. and G.Y. Shared a compound collection and analyzed data: A.M.D., M.P., and D.M.S. Contributed to biotransformation studies: K.P., A.S., and K.Y.R. Contributed to whole-cell activity work: A.S., C.S., D.Z., Y.L., J.R., and B.S.G. Applied chemi-informatic filters to the HTS dataset: L.G., B.C., and A.U. Helped distribute reagents across institutes: N.S. and Z.T. Contributed to the data analysis: C.B.C., B.S.G., K.Y.R., J.C.S., N.F., J.A., K.P., I.K., and C.N. Wrote the manuscript: A.S., S.O., I.K., K.P., and C.N. **Competing interests:** The authors declare that they have no competing interest. **Data and materials availability:** All data needed to evaluate the conclusions in the paper are present in the paper and/or the Supplementary Materials. Compounds synthesized for this study are available if supplies remain.

Submitted 14 July 2023
Accepted 9 February 2024
Published 15 March 2024
10.1126/sciadv.adj6406